Review article Open Access

Yin Huang, Yuecheng Shen, Changjun Min, Shanhui Fan and Georgios Veronis*

Unidirectional reflectionless light propagation at exceptional points

DOI 10.1515/nanoph-2017-0019
Received February 2, 2017; revised March 22, 2017; accepted March 31, 2017

Abstract: In this paper, we provide a comprehensive review of unidirectional reflectionless light propagation in photonic devices at exceptional points (EPs). EPs, which are branch point singularities of the spectrum, associated with the coalescence of both eigenvalues and corresponding eigenstates, lead to interesting phenomena, such as level repulsion and crossing, bifurcation, chaos, and phase transitions in open quantum systems described by non-Hermitian Hamiltonians. Recently, it was shown that judiciously designed photonic synthetic matters could mimic the complex non-Hermitian Hamiltonians in quantum mechanics and realize unidirectional reflection at optical EPs. Unidirectional reflectionlessness is of great interest for optical invisibility. Achieving unidirectional reflectionless light propagation could also be potentially important for developing optical devices, such as optical network analyzers. Here, we discuss unidirectional reflectionlessness at EPs in both parity-time (*PT*)-symmetric and non-*PT*-symmetric optical systems. We also provide an outlook on possible future directions in this field.

***Corresponding author: Georgios Veronis,** School of Electrical Engineering and Computer Science, Louisiana State University, Baton Rouge, LA 70803, USA; and Center for Computation and Technology, Louisiana State University, Baton Rouge, LA 70803, USA, e-mail: gveronis@lsu.edu
Yin Huang: Department of Optoelectrics Information Science and Engineering, School of Physics and Electronics, Central South University, Changsha, Hunan 410012, China; and Key Laboratory of Optoelectronic Devices and Systems of the Ministry of Education and Guangdong Province, Shenzhen University, Shenzhen 518060, China
Yuecheng Shen: Department of Biomedical Engineering, Washington University in St. Louis, One Brookings Drive, St. Louis, MO 63130, USA
Changjun Min: Key Laboratory of Optoelectronic Devices and Systems of the Ministry of Education and Guangdong Province, Shenzhen University, Shenzhen 518060, China
Shanhui Fan: E.L. Ginzton Laboratory, Stanford University, Stanford, CA 94305, USA

Keywords: invisibility; parity-time symmetry; exceptional points; waveguides; optical devices.

1 Introduction

Exceptional points (EPs), which are branch point singularities of the spectrum, associated with the coalescence of both eigenvalues and corresponding eigenstates, lead to interesting phenomena, such as level repulsion and crossing, bifurcation, chaos, and phase transitions in open quantum systems described by non-Hermitian Hamiltonians [1–4]. EPs have been studied in lasers [5], coupled dissipative dynamical systems [6], mechanics [7], electronic circuits [8], gyrokinetics of plasmas [9], and atomic as well as molecular systems [10]. In the past few years, EPs in non-Hermitian parity-time (*PT*)-symmetric systems have attracted considerable attention [11]. In quantum mechanics, non-Hermitian Hamiltonians may still possess entirely real energy spectra as long as they respect *PT*-symmetry. In general, the Hamiltonian $\boldsymbol{H}=\boldsymbol{p}^2/2+V(\boldsymbol{r})$, associated with a complex potential $V(\boldsymbol{r})$, is *PT*-symmetric as long as the complex potential satisfies the condition $V(\boldsymbol{r})=V^*(-\boldsymbol{r})$ [11]. However, once a non-Hermiticity parameter exceeds a certain threshold, the eigenvalues of the Hamiltonian cease to be all real. This threshold is associated with the appearance of the EP, where the eigenvalue branches merge and *PT*-symmetry breaks down. Based on the close analogy between the Schrödinger equation in quantum mechanics and the wave equation in optics, *PT*-symmetry in optics requires that $n(\boldsymbol{r})=n^*(-\boldsymbol{r})$, which implies that the real part of the refractive index $n(\boldsymbol{r})$ should be an even function of position, whereas the imaginary part must be an odd function [12, 13].

The constructed *PT*-symmetric optical structures with balanced gain and loss can lead to a range of extraordinary phenomena, including novel beam refraction [14, 15], power oscillation [16, 17], loss-induced transparency [18], nonreciprocal nonlinear light transmission [17, 19, 20], perfect absorption [21–23], teleportation [24], optical switching [25], optical tunneling [26], mode conversion [27], super scattering [28], and various other novel nonlinear effects [29–31]. In addition, there has been significant progress in using *PT*-symmetric periodic optical structures to attain unidirectional light reflectionlessness [12, 13]. In such structures, the reflection is zero when measured from one end of the structure at optical EPs and nonzero when measured from the other end.

Unidirectional reflectionlessness at EPs can be understood by considering a general two-port optical scattering system, as shown in Figure 1. The optical properties of this system can be described by the scattering matrix S defined by [32]

$$\begin{pmatrix} H_R^- \\ H_L^- \end{pmatrix} = S \begin{pmatrix} H_L^+ \\ H_R^+ \end{pmatrix} = \begin{pmatrix} t & r_b \\ r_f & t \end{pmatrix} \begin{pmatrix} H_L^+ \\ H_R^+ \end{pmatrix}, \tag{1}$$

where H_L^+ and H_R^+ are the complex magnetic field amplitudes of the incoming modes at the left and right ports, respectively. Similarly, H_L^- and H_R^- are the complex magnetic field amplitudes of the outgoing modes from the left and right ports, respectively. In addition, t is the complex transmission coefficient, whereas r_f and r_b are the complex reflection coefficients for light incidence from the left (forward direction) and from the right (backward direction), respectively. We note that, because *PT*-symmetric structures are in general reciprocal, the transmission coefficients in both directions must be the same [33]. However, the reflection coefficients from the left and right directions are not constrained by reciprocity and can therefore be different. We also note that the scattering matrix S as defined here [Equation (1)], which is in general nonsymmetrical, is different from the typical convention used in electromagnetics [22]. In general, the matrix S is non-Hermitian, and its corresponding complex eigenvalues are $\lambda_s^\pm = t \pm \sqrt{r_f r_b}$. Its eigenstates, which are $\Psi_\pm = \left(1, \pm\sqrt{\frac{r_f}{r_b}}\right)$ for $r_b \neq 0$, are not orthogonal. The two eigenvalues and the corresponding eigenstates can be coalesced and form EPs. Such non-Hermitian degeneracies represent scattering states with unidirectional reflectionless propagation in the forward ($r_f = 0$, $r_b \neq 0$) or backward ($r_b = 0$, $r_f \neq 0$) direction.

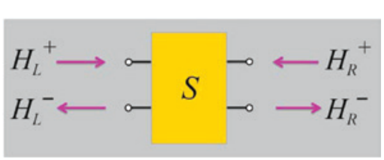

Figure 1: Scattering matrix S of a two-port optical system. H_L^+ and H_R^+ are the complex magnetic field amplitudes of the incoming modes at the left and right ports, respectively. Similarly, H_L^- and H_R^- are the complex magnetic field amplitudes of the outgoing modes from the left and right ports, respectively.

In the case of unidirectional reflectionless propagation in the forward direction ($r_f = 0$, $r_b \neq 0$), the scattering matrix S eigenvalues $\lambda_s^\pm$ coalesce into $\lambda_c = t$ and the eigenstates $\Psi_\pm$ coalesce into the only eigenstate $\Psi_c = (1,0)^T$. Because the scattering matrix eigenstates coalesce into the only eigenstate $\Psi_c = (1,0)^T$, they no longer form a complete basis. We note that the eigenstate Ψ_c corresponds, through Equation (1), to a well-defined physical scattering state with $(H_L^+, H_R^+) = \Psi_c = (1,0)^T$ and $(H_L^-, H_R^-) = \lambda_c \Psi_c = (t,0)^T$. In other words, the eigenstate corresponds to a state with unidirectional reflectionless propagation for light incident from the left. A similar discussion holds for the case of unidirectional reflectionless propagation in the backward direction ($r_b = 0$, $r_f \neq 0$).

The two complex eigenvalue solutions of the scattering matrix S construct a multivalued Riemann surface [1, 3]. They are on two branches of the Riemann surface. The two branches, $\lambda_s^\pm = t \pm \sqrt{r_f r_b}$, represent two superposition states between forward and backward light scatterings, including both transmission and reflection. The solutions of two branches coalesce and lead to EPs, corresponding to singularity points in the complex Riemann surface [1]. The reflection in both directions is due to the superposition of such two solutions [34]. At the EPs, light scattering is a destructive interference of two branch solutions. Therefore, the corresponding modal interference between two branch solutions at the EPs suppresses the reflection in one direction but not the other [34]. EPs exist in a larger family of non-Hermitian Hamiltonians [34]. Unidirectional reflectionless propagation can also be observed in non-*PT*-symmetric optical systems with unbalanced gain and loss [34].

In this paper, we review the fundamental physics and the latest developments on unidirectional reflectionless light propagation at EPs. In Section 2, we first review the unidirectional reflectionless propagation at EPs in *PT*-symmetric optical systems. Section 3 is devoted to reviewing unidirectional reflectionless propagation at EPs in non-*PT*-symmetric optical systems. Finally, in Section 4, we conclude this review and offer our perspectives on possible future directions in this field.

2 Unidirectional reflectionless propagation in *PT*-symmetric systems

To realize a *PT*-symmetric optical structure with unidirectional invisibility, Lin et al. used coupled mode theory (CMT) to theoretically investigate a 1D optical structure consisting of a periodic grating with refractive index distribution along the propagation direction $n(z)=n_0+n_1\cos(2\beta z)+in_2\sin(2\beta z)$ for $|z|<L/2$ (Figure 2A) [12]. This grating is embedded in a homogeneous medium having a uniform refractive index n_0 for $|z|>L/2$ (Figure 2A). Here, β is the grating wave number. The terms $n_1\cos(2\beta z)$ and $n_2\sin(2\beta z)$ correspond to the periodic distribution of the real and imaginary parts (gain and loss) of the complex refractive index in the grating, respectively. For *PT*-symmetric optical systems, the eigenvalues of the *S* matrix (Figure 1) must be either a unimodular ($|\lambda_s^{\pm}|=1$), or a nonunimodular inverse conjugate pair $\left[\lambda_s^{\pm}=\dfrac{1}{(\lambda_s^{\pm})^*}\right]$ [22]. In the former case, the system is in the exact *PT* phase, whereas, in the latter one, it is in the broken symmetry phase [21, 22, 35]. For the complex periodic structure considered in Figure 2A, the transition from one phase to another takes place when $n_1=n_2$. At $n_1=n_2$, the eigenvalues of the *S* matrix and their corresponding eigenvectors coalesce and form an EP, indicating that the phase transition takes place exactly at this EP. In fact, in quantum mechanics, the phase transition due to a non-Hermitian degeneracy is another phenomenon associated with EPs [36, 37].

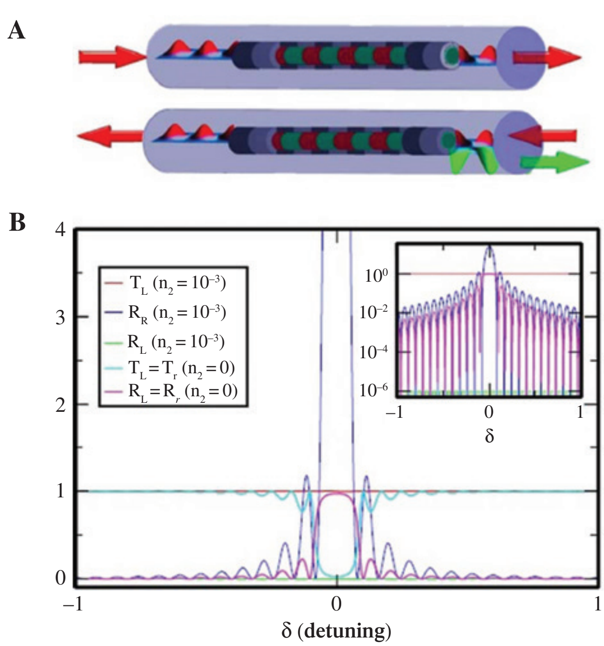

Figure 2: Unidirectional invisibility of a *PT*-symmetric Bragg scatterer.
(A) The wave entering from the left does not recognize the existence of the periodic structure and goes through the sample entirely unaffected. On the contrary, a wave entering the same grating from the right experiences enhanced reflection. (B) Exact numerical evaluation [from Equation (1)] of transmission *T* and reflection *R* coefficients for a Bragg grating for $n_0=1$, $n_1=10^{-3}$, $L=12.5\ \pi$, and $\beta=100$. In case of a *PT* grating, the system is at the EP when $n_1=n_2$. In this case, R_L is diminished (up to $n_{1,2}^{\ 2}\sim10^{-6}$; see inset) for a broad frequency band, whereas R_R is enhanced [12].

Figure 2B shows the transmission and reflection coefficients as a function of the detuning $\delta=\beta-k$, where $k=\omega n_0/c$. At $n_1=n_2$ (EP), the reflection in the left direction $R_L=|r_f|^2$ is zero, whereas the reflection in the right direction $R_R=|r_b|^2$ is nonzero. Meanwhile, the transmission ($T=|t|^2$) is unity, which implies that the Bragg scatterer is invisible when the light is incident from left (light propagating as if the Bragg scatterer is absent). Note that the transmitted wave cannot be detected from interference measurements, as the phase ϕ_t of the transmission coefficient *t* is zero at $n_1=n_2$ (EP). In addition, the transmission delay time $\tau_t=d\phi_t/dk$ is zero at $n_1=n_2$, which indicates that the time of flight of the light transmitted through a certain distance is the same whether there is a Bragg scatterer or not. Therefore, reflectionlessness in the proposed *PT*-symmetric Bragg scatterer results in invisibility. It is also clear that the reflection coefficients are symmetric, that is, $R_L=R_R$, when no gain or loss is included in the system ($n_2=0$). In addition, the generalized power representation $T+\sqrt{R_LR_R}$, relates all the elements in the scattering matrix *S* and is essentially the power summation of the superposition of the two eigenstates [Equation (1)] [38]. Note that the reflection of an incident wave from the left side of the structure is subunitary, whereas the reflection from the right side is superunitary. Therefore, $T+R_R$ in this system (Figure 2A) can be larger than one (Figure 2B) [38]. When the reflection in the forward and backward directions are equal, we obtain $T+\sqrt{R_LR_R}=T+R=1$, which is the power conservation relation for an optical system without gain or loss (Figure 2B).

Later on, Longhi reconsidered the scattering properties of this sinusoidal *PT*-symmetric Bragg scatterer (Figure 2A) using modified Bessel functions of the first kind [39]. His analytical results show that the unidirectional reflectionlessness only occurs for Bragg scatterers with short length *L* at EPs and breaks down for extremely long length scatterers. Note that the derivation of coupled-mode equations in Ref. [12] was based on multiscale asymptotic techniques and the rotating wave approximation [40]. Subsequently, Sarisaman demonstrated unidirectional reflectionlessness and invisibility in the TE and TM modes of a *PT*-symmetric slab system consisting of a separated pair of balanced gain and loss layers with a gap [41]. Kalish et al. reported that one-way invisibility could be obtained in randomly layered optical media with *PT*-symmetric refractive index [42]. Midya designed unidirectionally invisible complex optical crystals with balanced gain and loss based on nonrelativistic supersymmetry transformations [43]. Fu et al. demonstrated the existence of two EPs in a waveguide system consisting of zero-index materials with *PT* symmetry, which could induce unidirectional transparency [44]. Rivolta and Maes observed unidirectional visibility in a structure consisting of a waveguide and a finite chain of side-coupled resonators [45]. Fleury et al. constructed a unidirectional reflectionless optical system using two metasurfaces characterized by a *PT*-symmetric impedance distribution [46].

Regensburger et al. performed scattering experiments on a periodic *PT*-symmetric temporal Bragg scatterer by imposing a periodic phase modulation only within a finite time window [13]. Outside this time window, the periodic potential does not have an effect on light traveling, and the Bragg scatterer reflects light coming from both sides of the scatterer. When gain and loss are added to the phase modulation in a *PT*-symmetric fashion within the time window, unidirectional invisibility occurs at EPs. Hahn et al. first observed totally asymmetric diffraction in a *PT*-symmetric photonic lattice at EPs using vector-field holographic interference of two elliptically polarized pump beams on azobenzene-doped polymer thin films [47].

PT-symmetry in surface plasmon polaritons (SPPs) has been demonstrated by Yang and Mei [48]. SPPs, which are surface waves propagating along the interface between a metal and a dielectric [49], can concentrate electromagnetic energy at volumes of subwavelength scale and enable the manipulation of light beyond the diffraction limit [50–59]. Yang and Mei introduced a periodic *PT*-symmetric modulation on the effective refractive index of a metal-dielectric waveguide in the cylindrical coordinate system. After a coordinate transformation, they realized a 3D cylindrical unidirectional *PT*-cloak at EPs for SPPs. Zhu et al. have also demonstrated a one-way invisible cloak based on a transformed *PT*-symmetric optical potential at EPs [60].

Unidirectional reflectionlessness can also be attained in optical coupled-resonator systems at EPs [61, 62]. Jin et al. studied the scattering of rhombic ring form coupled resonators with enclosed synthetic magnetic flux [62]. The scattering center is a two-arm Aharonov-Bohm interferometer. The magnetic flux induces nonreciprocal tunneling phase. In the presence of balanced gain and loss, the rhombic ring structure is under reflection *PT*-symmetry, which induces asymmetric reflection and reciprocal transmission. The optical gain and loss in the coupled-resonator optical systems can be experimentally realized using InGaAsP quantum wells and chrome or graphene layers, respectively, on top of the resonator [63–67].

Feng et al. have demonstrated an approach that leads to unidirectional reflectionless light propagation in a microscale silicon-on-insulator (SOI) waveguide platform without using *PT*-symmetric structures with balanced gain and loss [68]. They used only purely passive materials without gain, which relaxes the requirements of the fabrication, as optical gain is difficult to achieve using conventional complementary metal-oxide-semiconductor silicon technology. As shown in Figure 3A, they introduced a periodic passive *PT*-symmetric modulation of the dielectric permittivity along the direction of propagation $\Delta\varepsilon = \cos(qz) - i\delta\sin(qz)$ [instead of $\varepsilon = \cos(qz) - i\delta\sin(qz)$] into the SOI waveguides. Here, δ controls the relative strength and phase between the sinusoidal and cosinusoidal modulations, and q is the wave vector of the fundamental mode at the wavelength of 1550 nm.

The eigenvalues of the S matrix of the structure in Figure 3A are both unimodular but with an additional attenuation term included in the system for $0<\delta<1$. For $\delta>1$, the eigenvalues are a nonunimodular inverse conjugate pair with the same attenuation term. Therefore, $\delta=1$ is the phase transition point corresponding to the EP, where both eigenvalues and eigenvectors become degenerate. Figure 3B and C shows that, at $\delta=1$, the reflection in the backward direction (R_b) is zero, whereas the reflection in the forward direction (R_f) approaches ~40% as the modulation length L increases.

For practical implementation, periodically arranged sinusoidal-shaped combo structures are applied on top of a Si waveguide embedded inside SiO_2 to mimic the passive *PT* modulation on a macroscopic scale, in which imaginary part modulation is implemented with 14 nm Ge/24 nm Cr structures and 51 nm Si layers are used for real part modulation (Figure 3D). Figure 3E shows the fabricated passive *PT*-symmetric waveguide. The sinusoidal-shaped combo structures are first patterned in polymethyl methacrylate (PMMA) by electron beam lithography followed by evaporation and lift-off of Si and Ge/Cr in two steps. After these steps, the Si waveguide is formed by electron beam lithography and dry etching. The measured reflection spectra of the fabricated passive waveguide are in agreement with the theoretical predictions (Figure 3F). Asymmetric light propagation in this passive system is associated with the fact that EPs exist in a larger family of non-Hermitian Hamiltonians [34]. Using a similar method, Feng et al. proposed a passive *PT*-symmetric metawaveguide on an SOI platform for asymmetric interferometric light-light switching with a weak control beam, which enables coherent perfect absorption of a strong signal beam, based on the asymmetric reflection of the metawaveguide near the EP [69]. The high ratio between the strong signal beam and the weak control beam is in contrast to previous approaches of controlling light in

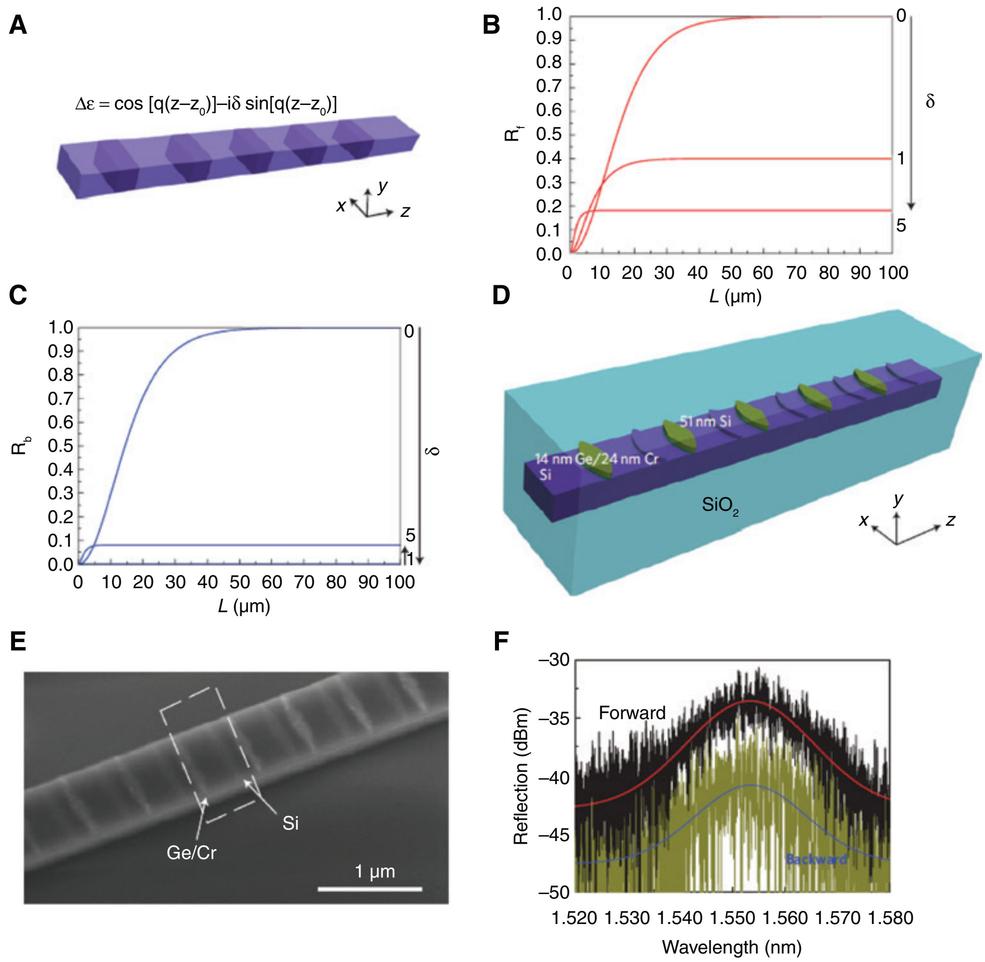

Figure 3: Optical properties of a designed passive unidirectional reflectionless *PT* metamaterial on an SOI platform.
(A) Schematic of the passive *PT* metamaterial on an SOI platform. Periodically arranged *PT* optical potentials with modulated dielectric permittivity of $\Delta\varepsilon = \cos(qz) - i\delta\sin(qz)$ $(4n\pi/q + \pi/q \le z \le 4n\pi/q + 2\pi/q)$ are introduced into an 800-nm-wide and 220-nm-thick Si waveguide embedded in SiO_2. The period is $4\pi/q = 575.5$ nm. (B and C) Dependences of reflectance of the passive *PT* metamaterial on the modulation length with different values of δ at the wavelength of 1550 nm in forward (B) and backward (C) directions, respectively. In contrast to the monotonic decrease in the forward direction, reflection in the backward direction first reaches a minimum value of $R_b = 0$ at $\delta = 1$ and then increases as δ becomes larger. (D) Periodically arranged 760-nm-wide sinusoidal-shaped combo structures are applied on top of an 800-nm-wide Si waveguide embedded inside SiO_2 to mimic *PT* optical potentials, in which imaginary part modulation is implemented with 14 nm Ge/24 nm Cr structures, and 51 nm Si layers are for real part modulation. The designed *PT* metamaterial consists of 25 sets of top-modulated combo structures with a period of 575.5 nm and a width of 143.9 nm for each sinusoidal-shaped combo. (E) SEM picture of the device, where the boxed area indicates a unit cell. (F) Measured reflection spectra of the device through the waveguide coupler for both directions over a broad band of telecom wavelengths from 1520 to 1580 nm. Red and blue curves are Gaussian fits of raw data in forward (black) and backward (green) directions, respectively [68].

all-optical active devices [22, 23, 70–74] and is promising for low-power next-generation optical networks.

In addition to the approach described above to achieve passive *PT*-symmetric SOI waveguides on a microscale platform, Jia et al. introduced a simple route to implement passive *PT* symmetry in the modal effective index of large-area (~cm^2) organic thin-film waveguides [75]. They used interference lithography to write a sinusoidal grating profile into a thin film of photoresist and deposit high extinction coefficient blue pigment copper phthalocyanine (CuPc) to coat the "windward" grating facets (Figure 4A). This arrangement results in a modal effective index with a passive *PT*-symmetric profile of the form $\Delta\tilde{n}_{\mathrm{eff}}(z) \approx (\Delta n_{\mathrm{eff}}/2)[1+\cos(qz)] + i(\Delta k_{\mathrm{eff}}/2)[1-\sin(qz)]$ for the fundamental guided mode. Figure 4B shows scanning electron micrographs (SEMs) of a fabricated composite waveguide before (top panel) and after (bottom panel) planarization of a top photoresist layer.

The optical property of the passive *PT*-symmetric waveguide is investigated using Kretschmann-coupled

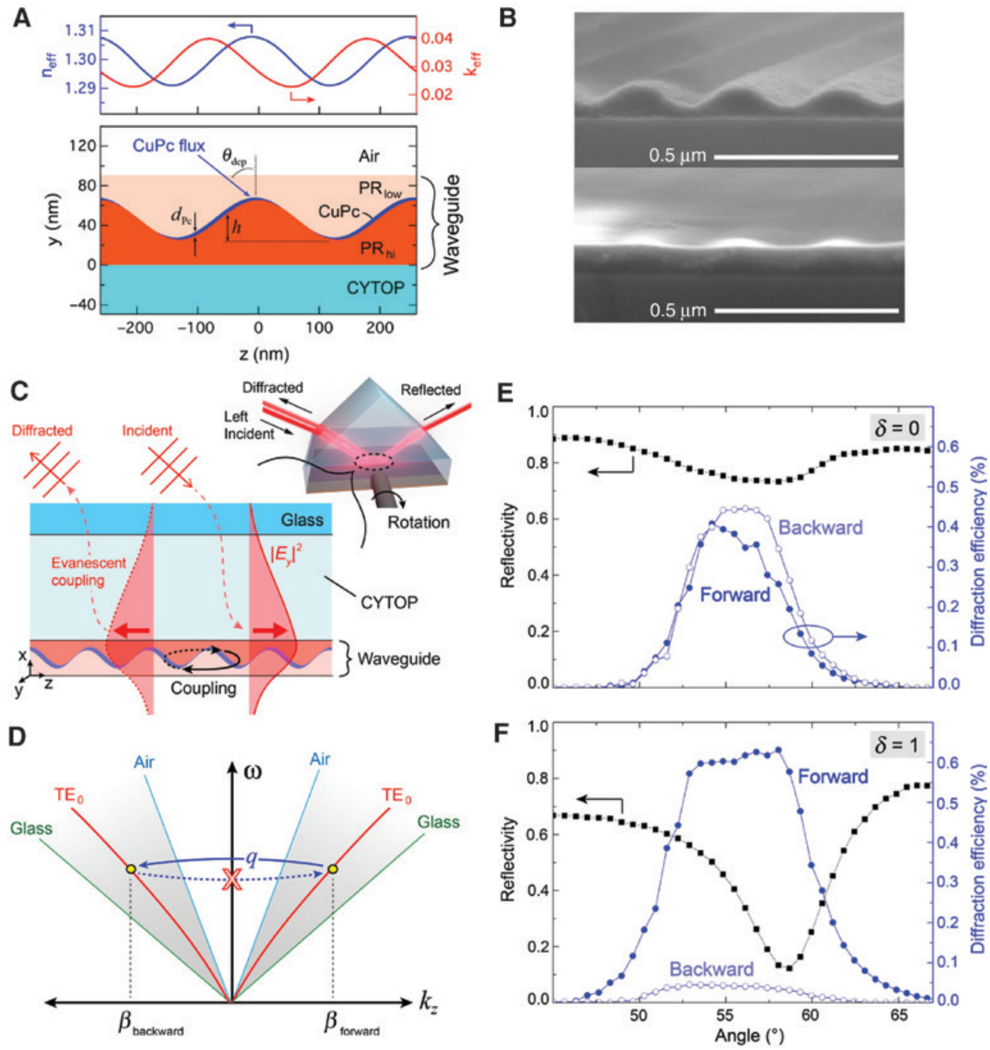

Figure 4: Unidirectional reflectionlessness of passive *PT*-symmetric organic thin-film waveguides.
(A) Waveguide composition calculated to support the fundamental leaky TE mode together with its corresponding position-dependent complex effective index $n_{eff}+ik_{eff}$ displayed in the top panel. (B) Cross-sectional SEM images of a typical CuPc-coated photoresist grating before (top) and after (bottom) planarization with the top photoresist layer. Faint contrast between the upper and lower photoresist layers remains visible in the bottom panel, confirming that the internal grating structure is maintained. (C) Diagram showing the optical measurement setup, where a laser beam is Kretschmann coupled into the leaky TE_0 mode supported by the composite waveguide layer. The intensity of the 0 order reflected and –1 order diffracted beam is measured as a function of incidence angle for forward and backward illumination corresponding to light incident on the left and right sides of the prism, respectively. (D) Dispersion diagram illustrating the process of unidirectional scattering within the complex index modulated waveguide that occurs at its EP. (E) Reflectivity and –1 order diffraction efficiencies measured as a function of incidence angle (in the glass substrate) for a bare waveguide with no CuPc. The diffracted intensities for forward and backward incidence peaks near the Littrow condition ($\theta_{inc}\sim 56°$), which is designed to coincide with resonant in-coupling to the waveguide mode marked by the reflectivity dip. (F) The same measurement carried out for a waveguide with CuPc ($d_{PC}=6$ nm, $\theta_{dep}=55°$) targeted to achieve $\delta\approx 1$ [75].

diffraction in Littrow [76]: first, the incident laser beam is evanescently coupled into the fundamental TE mode of the composite waveguide; then, the reverse-going waveguide mode is generated by grating reflection and subsequently evanescently coupled out to air (Figure 4C). Thus, measuring the diffraction efficiency, defined as $|E_{dif}/E_{inc}|^2$, for left and right incident light provides a proxy probe of the forward- and backward-going modal reflectivity within the waveguide. Here, E_{dif} and E_{inc} are the incident plane wave and diffractive wave amplitudes, respectively. At EPs, light in-coupled into the forward-going (left to right) mode can scatter into the backward-going (right to left) mode, giving rise to Littrow diffraction but not vice versa (Figure 4D).

As shown in Figure 4E, when $\delta=\Delta k_{eff}/\Delta n_{eff}=0$ (neither gain nor loss is included in the waveguide layer), the measured diffraction efficiency as a function of incidence angle for a TE-polarized 640 nm probe beam shows that the backward and forward Littrow diffraction efficiencies are similar. In contrast, at the EP, where $\delta = 1$, the backward Littrow diffraction efficiency is almost suppressed (Figure 4F). The reflectivity in the backward and forward directions is equal even in the presence of gain or loss. This is similar to the transmission in the structure of Figure 2B, which is the same in both directions regardless of the presence of gain or loss (Figure 2B). In addition, Yan and Giebink exploited vapor-deposited organic small molecules as a platform to realize passive *PT*-symmetry breaking and demonstrated unidirectional reflectionlessness at EPs in a composite organic thin film via complex refractive index modulation [77]. Zhu et al. designed a passive *PT*-symmetric grating with asymmetric diffraction arising from the spontaneous *PT*-symmetry breaking at EPs in a wide range of incidence angles [78].

The use of gain media in optical waveguides can lead to active optical devices and to material loss compensation [79–83]. Hahn et al. investigated the unidirectional reflectionlessness at EPs in *PT*-symmetric gratings based on active dielectric-loaded long-range SPP (DL-LRSPP) waveguides [84]. To obtain a *PT*-symmetric profile, they designed a step-in-width grating structure consisting of a thin Ag stripe on an active polymer bottom cladding with an active polymer ridge (Figure 5A). The polymer used is PMMA doped with IR140 dye.

Normally, in a typical waveguide, it is impossible to achieve a *PT*-symmetric profile because both the real (n_R) and the imaginary (n_I) parts of the effective index change monotonically with the geometric parameters. Thanks to the coupling between the fundamental mode and an asymmetric high-order mode of the waveguide, when the ridge width is within specific ranges, the effective index

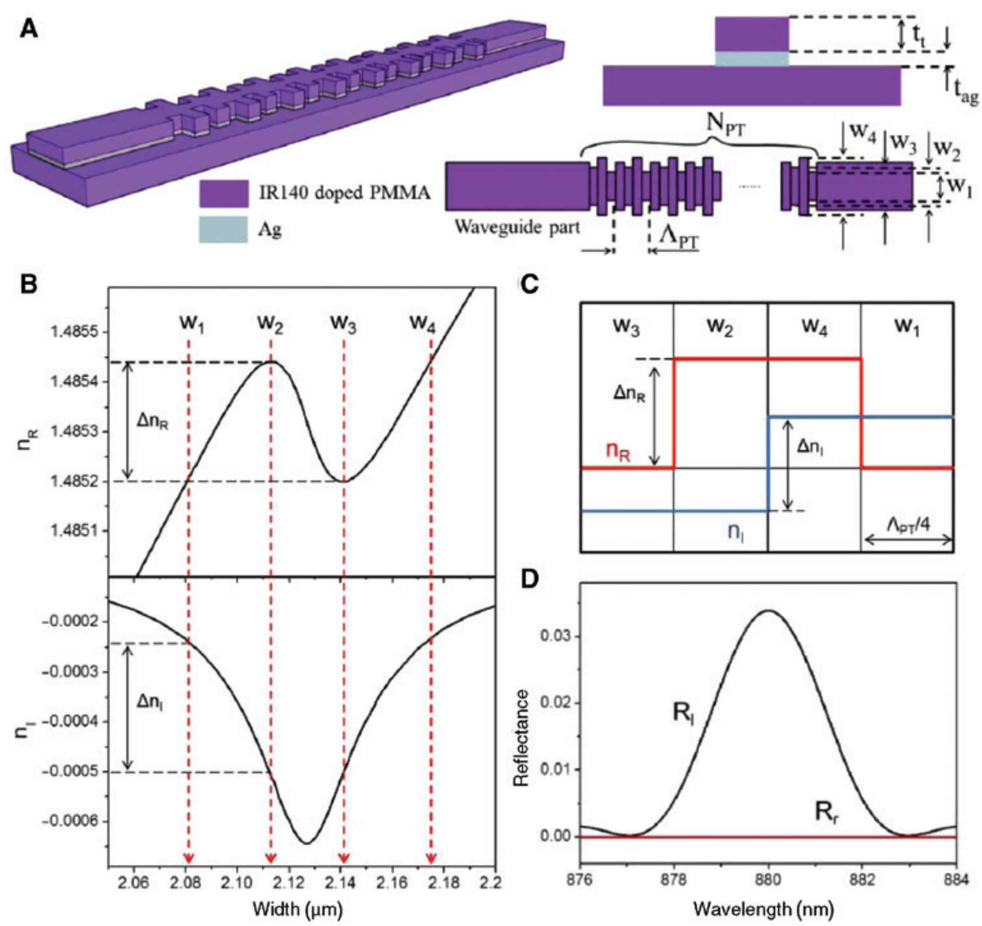

Figure 5: Optical properties of a designed passive unidirectional reflectionless DL-LRSPP *PT*-symmetric grating structure. (A) 3D view of a DL-LRSPP *PT*-symmetric grating structure. (B) Real and imaginary parts of effective index near the n_R crossing region of the ss_b^0 (fundamental) and sa_b^3 (asymmetric high-order) modes. Vertical red dashed lines indicate four widths selected for a *PT*-symmetric grating. (C) Schematic of the real and imaginary index distribution within one period. (D) Reflectance from the left side R_l and the right side R_r of a passive *PT*-symmetric grating operating at the EP [84].

of the DL-LRSPP waveguide has the potential to achieve a *PT*-symmetric profile. Figure 5B shows the effective index of the DL-LRSPP waveguide without gain as a function of the ridge width for a 35-nm-thick Ag stripe at a wavelength of 880 nm. One observes a large dip in the imaginary part of the effect index n_I and a peak then a dip in the real part of the effect index n_R. By arranging four widths within one step-in-width grating period in the sequence w_3, w_2, w_4, w_1, a passive *PT*-symmetric profile is obtained (Figure 5A and C). The thickness of the Ag stripe $t_{ag}=35$ nm was chosen to have $\Delta n_R=\Delta n_I$, which corresponds to an EP. Figure 5D shows the unidirectional reflection light propagation in such a *PT*-symmetric grating at its EP. When the gain of IR140-doped PMMA is included to make the average value of n_I zero or positive, the maximum reflection in the left direction (R_l) is greatly enhanced, and the grating can even become an active *PT*-symmetric grating. Moreover, by placing a gain waveguide within a cavity formed by concatenating two gratings with opposite nonreflective ends, a high-performance laser can be created at EPs [85].

In all cases presented above, to achieve *PT* symmetry, the dielectric permittivity profile is chosen so that $\varepsilon(z)=\varepsilon^*(-z)$, whereas the magnetic permeability is equal to the one of free space ($\mu=\mu_0$). If, however, magnetic materials ($\mu\neq\mu_0$) are considered, a similar requirement must be imposed on the magnetic permeability, that is, $\mu(z)=\mu^*(-z)$, to satisfy the *PT* symmetry condition $n(z)=\sqrt{\varepsilon(z)\mu(z)}=\sqrt{\varepsilon^*(-z)\mu^*(-z)}=n^*(-z)$ [86]. Interestingly, Li et al. explored the possibility of cross-matching $\varepsilon(z)$ to $\mu^*(-z)$, namely, $\varepsilon(z)=\mu^*(-z)$, to establish *PT* symmetry [87]. More specifically, they investigated a 1D photonic crystal (PhC) consisting of alternating purely dielectric slabs with $\varepsilon_1=2.25+i\gamma$, $\mu_1=1$ and purely magnetic slabs with $\mu_2=2.25-i\gamma$, $\varepsilon_2=1$ (Figure 6A). These two types of media have matched gain and loss coefficients. Note that $n_1=\sqrt{\varepsilon_1\mu_1}=\sqrt{\varepsilon_2^*\mu_2^*}=n_2^*$, so that the spatial *PT*-symmetry still holds.

Figure 6B and C shows the forward and backward reflection spectra, respectively, as a function of γ. The dips (red color in Figure 6B), reaching a value of zero, correspond to unidirectional reflection. To provide further insight into the unidirectional character in reflection, the eigenvalue behavior of constitutive matrix C^{-1} against γ is shown in Figure 6D. The optical property of a single unit cell can be described by the constitutive matrix C^{-1}

$$\begin{pmatrix} H_{y2}-H_{y1} \\ E_{x2}-E_{x1} \end{pmatrix} = \frac{\mathrm{i}k_0 a}{2} C^{-1} \begin{pmatrix} E_{x2}+E_{x1} \\ H_{y2}+H_{y1} \end{pmatrix}, \tag{2}$$

where E_{x1}, H_{y1} are the fields on the left side of the cell, E_{x2}, H_{y2} are the fields on the right side, and a is the lattice constant. The constitutive matrix C^{-1} can be written in terms

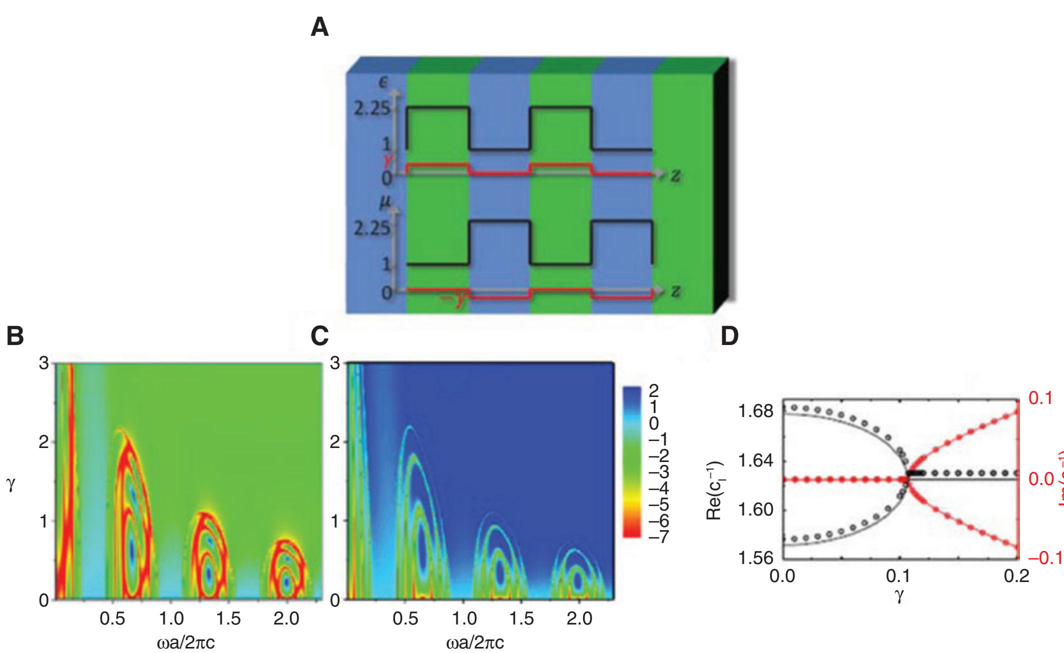

Figure 6: Unidirectional reflectionlessness of a *PT*-symmetric 1D PhC with cross-matching $\varepsilon(z)$ to $\mu^*(-z)$.
(A) Permittivity (ε) and permeability (μ) profiles of a 1D PhC stacking alternating purely dielectric slabs with $\varepsilon=2.25+i\gamma$ and purely magnetic slabs with $\mu=2.25-i\gamma$ with equal filling ratio and varying γ. (B) Forward and (C) backward reflectance (in natural log scale) for the PhC in (A) with a finite thickness of four unit cells. (D) Splitting of eigenvalues of the effective constitutive matrix C^{-1}. The scattered symbols (solid lines) are the numerical results (analytical effective medium results) [87].

of the S matrix [Equation (1)] of a single unit cell through a bilinear transformation

$$C^{-1}=\frac{2}{ik_0a}B\frac{S-I}{S+I}B^{-1},\ \text{with}\ I=\begin{pmatrix}1&0\\0&1\end{pmatrix}\ \text{and}\ B=\begin{pmatrix}1&1\\1&-1\end{pmatrix}. \quad (3)$$

Because unidirectional reflectionlessness occurs at an EP of the scattering matrix S, we can equivalently study the eigenvalue behavior of the matrix C^{-1}. The eigenvalues of matrix C^{-1} are pairs of two purely real numbers for $\gamma<0.107$, coincide at an EP for $\gamma=0.107$, and then split into a complex conjugate pair (Figure 6D). This eigenvalue behavior is equivalent to the transition of PT-symmetric Hamiltonians in quantum mechanics from the PT-symmetric phase to the PT-broken phase [11, 13, 88, 89]. The EP of the constitutive matrix C^{-1} is actually the EP of the S matrix, which leads to the unidirectional reflectionless behavior shown in Figure 6B and C.

When more material potentials, such as the magnetic permeability, are considered, additional degrees of freedom exist in establishing PT symmetry. An antisymmetric PT-photonic structure under combined PT operations, i.e. $n(-z)=-n^*(z)$, with balanced positive- and negative-index materials, has been reported, where the magnetic permeability was required to satisfy $\mu(-z)=-\mu(z)$ [90]. Studies showed that light propagation in optical lattices of driven cold atoms with PT-antisymmetric susceptibilities, i.e. $\chi(z)=-\chi^*(-z)$, exhibited EPs (also known as non-Hermitian degeneracies), at which complete unidirectional reflectionless light propagation was observed [91, 92].

In addition, a few recent studies of multidimensional PT-symmetric systems have demonstrated intriguing properties not found in 1D PT-symmetric systems, such as conical diffraction, third-order EPs, continuous rings of EPs, and rotating input by asymmetric coupling between wave vectors [14, 93–98]. Most recently, Fan et al. considered 2D PT-symmetric PhCs, whose non-Hermitian primitive cell is an integer multiple of the primitive cell of the underlying Hermitian system [15]. Similar to many other low-dimensional PT systems, PT-symmetric PhCs can also exhibit unidirectional reflection behavior when light comes from the left and right sides of PhCs.

3 Unidirectional reflectionless propagation in non-*PT*-symmetric systems

As we have mentioned in the previous sections, there is a large family of non-Hermitian Hamiltonians that can produce merged branches of eigensolutions through accidental degeneracy [34]. Therefore, can a non-PT-symmetric system, in which the relation $n(-z)=n^*(z)$ for the refractive index profile does not hold, lead to asymmetric reflection? It has been reported that unidirectional reflectionlessness can be realized in a two-layer non-PT-symmetric slab structure by tuning both the real and imaginary parts of the refractive index of each layer at EPs [99].

Moreover, Horsley et al. completely suppressed scattering in one direction in a planar inhomogeneous dielectric structure, in which the spatial distributions of the real and imaginary parts of the dielectric permittivity are related by Kramers-Kronig relations [100]. Specifically, they considered a monochromatic electromagnetic wave propagating in the x–y plane within a medium with a positive background contribution ε_b plus a spatially varying part α in the dielectric permittivity ε: $\varepsilon(x)=\varepsilon_b+\alpha(x)$ (Figure 7A).

If we expand the scattered field induced by the variation $\alpha(x)$ as a series, $e_s=\sum_n e_s^{(n)}$, and solve the Helmholtz equation for the TE polarization, the first and nth terms in this series can be expressed as

$$e_s^{(1)}(x)=-E_0k_0^2\int\frac{\mathrm{d}k}{2\pi}G(k)\tilde{\alpha}(k-K)\mathrm{e}^{\mathrm{i}kx}, \quad (4)$$

$$e_s^{(n)}(x)=-k_0^2\int\frac{\mathrm{d}k}{2\pi}\int\frac{\mathrm{d}k'}{2\pi}G(k)\tilde{\alpha}(k-k')\,\tilde{e}_s^{(n-1)}(k')\mathrm{e}^{\mathrm{i}kx}, \quad (5)$$

where $\tilde{\alpha}$ is the spatial Fourier transform of $\alpha(x)$, $G(k)$ is the retarded Green function, $K=(\varepsilon_bk_0^2-k_y^2)^{1/2}$ and k_y determines the angle of incidence. If $\tilde{\alpha}(k<0)=0$, then the first item $e_s^{(1)}(x)$ is composed of only right-going waves for any value of K or, in other words, for any angle of incidence. Based on Equation (5), every successive term also contains only right-going waves if $e_s^{(1)}$ is composed of right-going waves and $\tilde{\alpha}(k<0)=0$. Interestingly, the requirement $\tilde{\alpha}(k<0)=0$ can be satisfied when the permittivity profile $\alpha(x)$ is holomorphic (analytic) in the upper half complex plane, i.e. $\mathrm{Im}(x)\geq 0$, and is of Kramers-Kronig type [101]:

$$\mathrm{Re}[\alpha(x)]=\frac{1}{\pi}\mathrm{P}\int_{-\infty}^{\infty}\frac{\mathrm{Im}[\alpha(s)]}{s-x}\mathrm{d}s, \quad (6)$$

where P is the principal part of the integral. We consider a specific example with $\alpha(x)=A\frac{\mathrm{i}-x/\xi}{1+(x/\xi)^2}$. The overall permittivity profile of the medium is then

$$\varepsilon(x)=\varepsilon_\mathrm{b}+A\frac{\mathrm{i}-x/\xi}{1+(x/\xi)^2}, \quad (7)$$

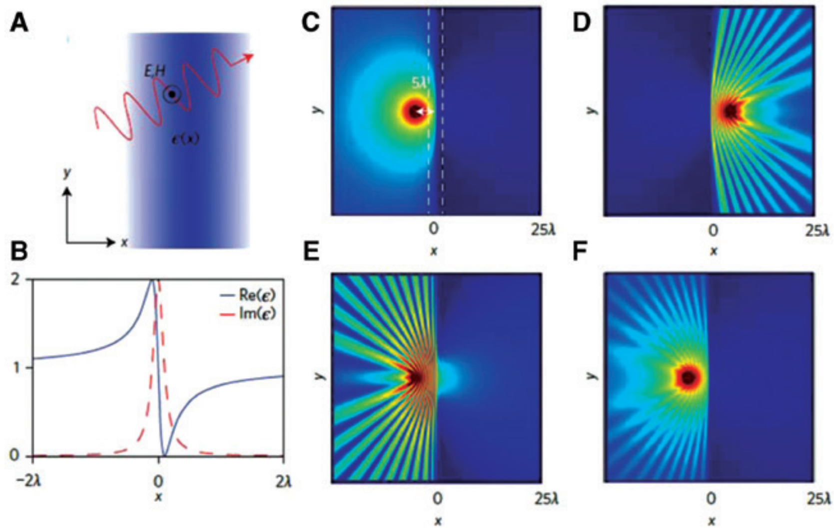

Figure 7: Unidirectional reflectionlessness of a planar inhomogeneous dielectric structure in which the spatial distributions of the real and imaginary parts of the dielectric permittivity are related by Kramers-Kronig relations.
(A) A wave propagating in the x–y plane in an inhomogeneous medium with permittivity $\varepsilon(x)$ (indicated by blue shading). The TE polarization has an electric field pointing only along z and the TM polarization has a magnetic field pointing only along z. When the real (blue) and imaginary (red) parts of the permittivity are related to one another by the Kramers-Kronig relations (as in B), then the reflection vanishes for all angles of incidence. (B) Permittivity profile $\varepsilon(x)$ given by Equation (7) for parameters $A=2$ and $\xi=0.1\lambda$ with $\lambda=2\pi/k_0$. (C and D) Absolute values of the electric field of a line source placed at positions $x=-5\lambda$ (C) and $x=+5\lambda$ (D) in the permittivity profile. The region between the vertical dashed lines in (C) indicates the region plotted in (B). (E and F) As in (C and D), with identical parameters, but taking only the real (E) and imaginary (F) parts of the permittivity. The absence of any oscillations in (C) shows that the reflection is completely suppressed for incidence from the left for all incident angles [100].

which is plotted in Figure 7B. Here, ξ and A set the spatial scale and amplitude of the profile, respectively.

The one-way scattering behavior is confirmed in Figure 7C and D, which show electric field profiles for a point source placed at either side of $x=0$. The absence of reflection is clearly observed when light is incident from the left. Figure 7E and F shows the electric field when only the real (Figure 7E) or the imaginary (Figure 7F) parts of the permittivity profile [Equation (7)] are considered. In fact, if the imaginary part of $\alpha(x)$ is set to be symmetric about $x=0$, then the real part calculated based on Equation (6) is antisymmetric and vice versa. Thus, the spatial Kramers-Kronig relations can generate permittivity profiles that exhibit PT-symmetry [$\alpha(-x)=\alpha^*(x)$]. In other words, compared to the specific class of PT-symmetric complex profiles, the permittivity profiles associated with Kramers-Kronig relations are more general nonreflecting profiles, which can achieve unidirectional reflectionlessness at EPs.

The refractive index modulation profiles that we have considered so far for synthesizing PT-symmetric or non-PT-symmetric optical structures require careful tuning of both the real and imaginary parts of the refractive index of the constituent materials, which increases the difficulty in practical realization. Therefore, the question arises as to whether it is possible to achieve asymmetric reflection in a non-PT-symmetric system by tuning only the real or only the imaginary part of the refractive index of the material. Feng et al. recently demonstrated unidirectional reflectionless light transport at EPs in a conventional large-sized nonperiodic multilayer structure, which was fabricated by alternating thin film depositions of lossy amorphous silicon and lossless silica layers on a cleaned glass wafer using plasma-enhanced chemical vapor deposition (43 nm silica/9 nm silicon/26 nm silica/23 nm silicon; Figure 8A) [102]. The refractive index of silica at the wavelength of interest is 1.46, and the complex refractive index of amorphous silicon is $4.86+i\gamma$, so that the proposed structure is clearly non-PT-symmetric. Using the transfer matrix theory [103], one can show that, by modulating only the imaginary part of the refractive index of amorphous silicon, the eigenvalues of the S matrix of this multilayer system coalesce and form an EP when $\gamma=-0.65$. The reflection spectra of the structure for both forward and backward directions were numerically calculated and experimentally measured, as shown in Figure 8B and C, respectively. Unidirectional reflectionless light transport is clearly observed around the wavelength of 520 nm, where the reflection in the forward direction is significantly suppressed due to the existence of the EP.

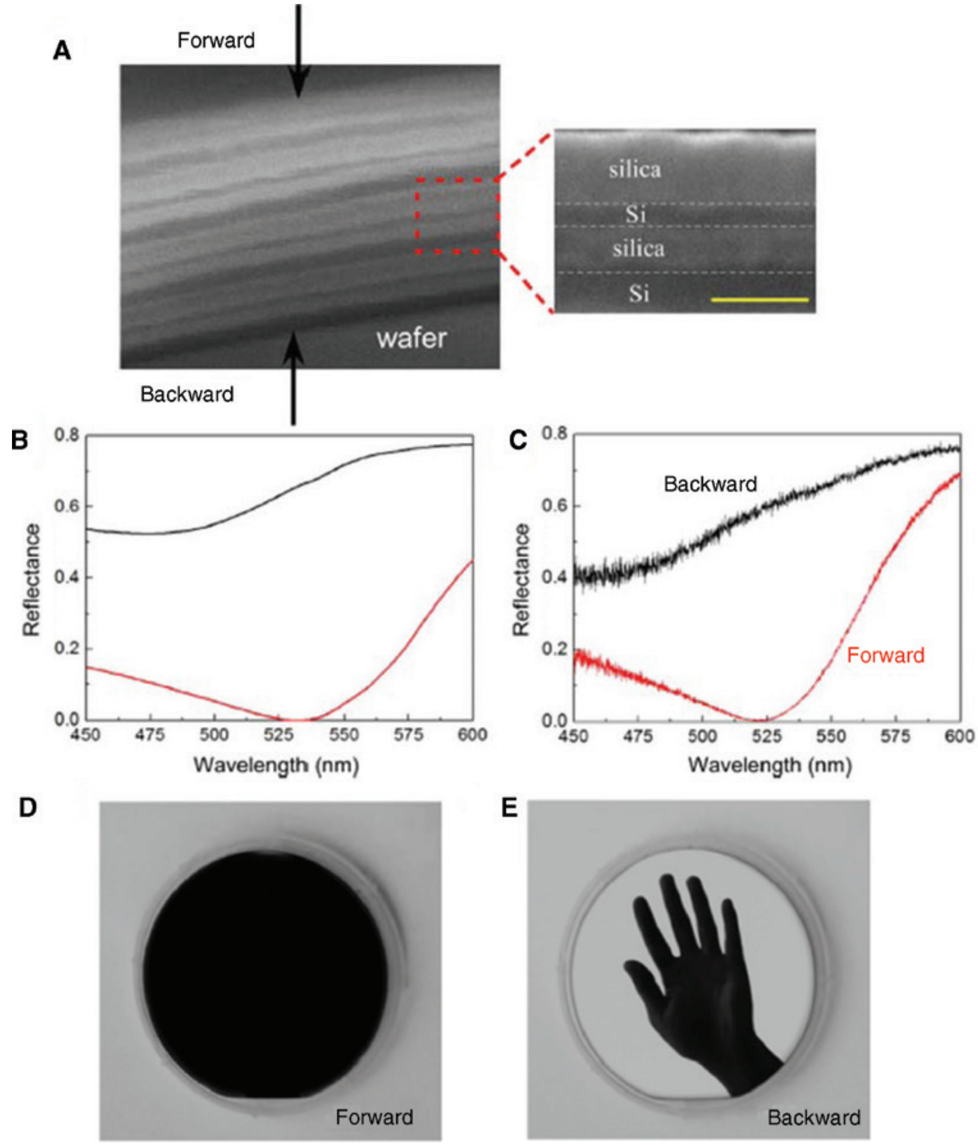

Figure 8: Unidirectional reflectionlessness of a non-*PT*-symmetric large-sized nonperiodic multilayer structure consisting of lossy amorphous silicon and lossless silica layers.
(A) SEM pictures of the cross-section of the fabricated EP structure. The scale bar corresponds to 50 nm. (B and C) Numerically calculated and experimentally measured reflection spectra of the EP structure from 450 to 600 nm, respectively, for both forward (red) and backward (black) incidence. (D and E) Photographs of the wafer-scale EP structure in forward and backward directions, respectively, with a 10-nm band-pass filter centered at the wavelength of 520 nm [102].

In the presence of loss, this optical system is analogous to open quantum systems that are subjected to dissipation and characterized by complex non-Hermitian Hamiltonians. Thus, the existence of EPs in this purely lossy non-*PT*-symmetric optical system also provides an opportunity to control the unidirectional reflection of light. Because of the associated unidirectional reflectionless light propagation at the EP, this large-sized non-*PT*-symmetric multilayer structure can form imaging in reflection under sunlight illumination only from the backward direction. An image formed in the backward direction is shown in Figure 8E, whereas an image cannot be formed in the forward direction due to the nonreflecting behavior of the structure (Figure 8D).

A couple of subsequent studies showed theoretically that unidirectional reflectionless light propagation can be realized in similar two-layer non-*PT*-symmetric lossy dielectric slab structures with modulation of the imaginary part of the refractive index of each slab [104, 105]. Ge and Feng further pointed out that an optical reciprocity-induced symmetry, which is related to the amplitude ratio of the incident waves in the scattering eigenstates, can lead to an EP. Because optical reciprocity holds in general and does not rely on *PT* symmetry, the unidirectional reflectionlessness at EPs can be obtained in optical systems with unbalanced gain and loss and even in the absence of gain [105]. In addition, Kang et al. designed a non-*PT*-symmetric ultrathin metamaterial to exhibit one-way zero reflection at EPs [106].

Forming an EP of the *S* matrix through tuning the geometric parameters of a structure rather than the refractive index profile was proposed in a non-*PT*-symmetric plasmonic waveguide-cavity system consisting of two metal-dielectric-metal (MDM) stub resonators side coupled to an MDM waveguide (Figure 9A) [107]. Tuning the geometry rather than the refractive index can reduce the difficulty

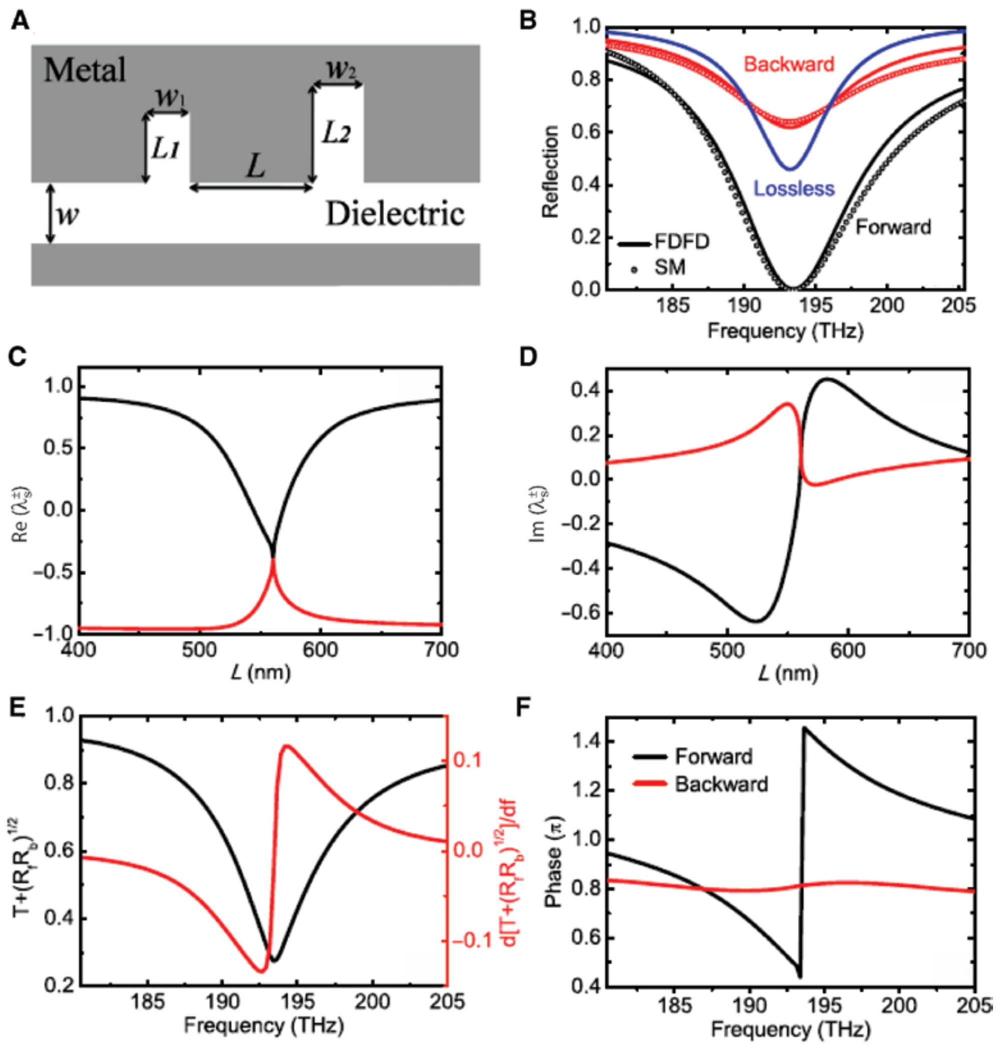

Figure 9: Unidirectional reflectionlessness of a non-*PT*-symmetric system consisting of a MDM plasmonic waveguide side coupled to two MDM stub resonators.
(A) Schematic of an MDM plasmonic waveguide side coupled to two MDM stub resonators. (B) Reflection spectra for the structure of (A) calculated for both forward and backward directions using the finite-difference frequency-domain (FDFD) method (solid lines) and the scattering matrix theory (circles). Results are shown for $w=50$ nm, $w_1=20$ nm, $w_2=100$ nm, $L_1=175$ nm, $L_2=365$ nm, and $L=561$ nm. Also shown are the reflection spectra calculated using FDFD for lossless metal (blue solid line). (C and D) Real and imaginary parts of the eigenvalues of the scattering matrix S as a function of the distance L between the two MDM stub resonators. The black and red lines correspond to eigenvalues $\lambda_s^+=t+\sqrt{r_f r_b}$, and $\lambda_s^-=t-\sqrt{r_f r_b}$, respectively. All other parameters are as in (B). (E) Spectra of the generalized power $T+\sqrt{R_f R_b}$ (black) and of the differential generalized power (red), defined as the derivative of the generalized power with respect to frequency $d\left[T+\sqrt{R_f R_b}\right]/df$, calculated using FDFD. All parameters are as in (B). (F) Phase spectra of the reflection coefficients in the forward (r_f, black) and backward (r_b, red) directions. All parameters are as in (B) [107].

in the experimental realization of such structures. Among different plasmonic waveguide structures, MDM plasmonic waveguides are of particular interest [108–116], because they support modes with deep subwavelength scale over a very wide range of frequencies extending from DC to visible [117] and are relatively easy to fabricate [118, 119]. The waveguide widths w, w_1, and w_2 are set to be 50, 20, and 100 nm, respectively (Figure 9A). The metal is silver and the dielectric is air. To obtain unidirectional reflectionless propagation, the MDM stub lengths L_1, L_2, as well as the distance between the stubs L, are optimized using the scattering matrix theory [120, 121] to minimize the amplitude of the reflection coefficient in the forward direction $|r_f|$ at the optical communication wavelength of $\lambda_0 = 1.55$ μm. Note that, if one tunes the refractive index of a material to form an EP, the optimized refractive index will be complex. However, if one tunes the geometric parameters to obtain an EP, these parameters are restricted to be purely real.

Figure 9B shows the reflection spectra for the structure of Figure 9A calculated for both forward and backward directions for $L_1 = 175$ nm, $L_2 = 365$ nm, and $L = 561$ nm. The results verify that the optimized structure of Figure 9A is unidirectional reflectionless at $f = 193.4$ THz ($\lambda_0 = 1.55$ μm). Figure 9C and D shows the real and imaginary parts, respectively, of the eigenvalues $\lambda_s^{\pm}$ of the scattering matrix S [Equation (1)] as a function of the distance L between the two MDM stub resonators. We observe that the real and imaginary parts of the two eigenvalues indeed collapse for $L = 561$ nm. As discussed above, this is the optimal distance between the two stubs, which minimizes the reflection in the forward direction. In Figure 9C and D, we observe the level repulsion in the real parts of the eigenvalues, as well as the level crossing in their imaginary parts, which resembles a system also described by a non-Hermitian Hamiltonian matrix consisting of two coupled damped oscillators [4]. In open quantum systems, a repulsion (crossing) for the real part of the energy and a crossing (repulsion) for the imaginary part of the energy in the 2D complex energy plane are required around EPs [3, 4]. Unlike the Hermitian case, the levels approach each other in the form of a cusp rather than a smooth approach because of the plain square-root behavior of the singularity (Figure 9C) [1, 4].

Similar to other classical optical systems that have EPs [102], we observe that a generalized power decreasing phase and a generalized power increasing phase are divided by the EP at $f = 193.4$ THz (Figure 9E). In addition, an abrupt phase change in the differential generalized power spectrum is observed at the EP as well (Figure 9E). These results are essentially due to the fact that the reflection coefficient in the forward direction r_f approaches zero at the EP. Figure 9F shows that the phase of the reflection coefficient in the forward direction undergoes an abrupt π jump, when the frequency is crossing over the EP, which actually resembles the phase transition from the *PT*-symmetric phase to the *PT* broken phase in optical *PT*-symmetric systems [12, 13, 17, 38, 102, 104]. Such an abrupt π-phase jump in the reflection coefficient in the forward direction confirms the existence of the EP in this plasmonic system and that the unidirectional reflectionlessness in the system is directly associated with this EP. In contrast, the phase of the reflection coefficient in the backward direction does not undergo an abrupt jump and varies smoothly with frequency. In addition, the reflection is not unidirectional if the system is lossless (Figure 9B). This is different from other classical optical analogues of quantum systems, such as the plasmonic analogue of electromagnetically induced transparency [122, 123], which can be realized in both lossless and lossy optical systems. In addition, the formation of an EP and the resulting unidirectional reflectionlessness can also be implemented using plasmonic waveguide-cavity systems based on other plasmonic two-conductor waveguides, such as 3D plasmonic coaxial waveguides [124, 125].

Unlike *PT*-symmetric systems, most non-*PT*-symmetric optical systems with modulation of the real or the imaginary part of the refractive index of the material typically exhibit unidirectional reflectionless propagation only within a very narrow wavelength range around the EP (see, for example, Figures 8C and 9B) [102, 104–107]. This is especially true for nonperiodic non-*PT*-symmetric systems, which are relatively easy to fabricate and more compact. Although Yang et al. demonstrated broadband unidirectional reflectionless light transport at an EP in a periodic ternary-layered structure consisting of lossy and lossless dielectrics [126], large-sized periodic structures are not easy to implement in densely integrated optical chips.

A compact non-*PT*-symmetric plasmonic waveguide-cavity system consisting of two MDM stub resonators with unbalanced gain and loss side coupled to an MDM waveguide was recently theoretically investigated (Figure 10A) [127]. This non-*PT*-symmetric structure can exhibit unidirectional reflectionlessness in the forward direction at $\lambda_0 = 1.55$ μm. Moreover, light reflection in the forward direction in this system is close to zero in a broad wavelength range.

Using the temporal CMT [128, 129], it can be shown that the unidirectional reflectionlessness condition coincides with the broadband near-zero reflection condition if

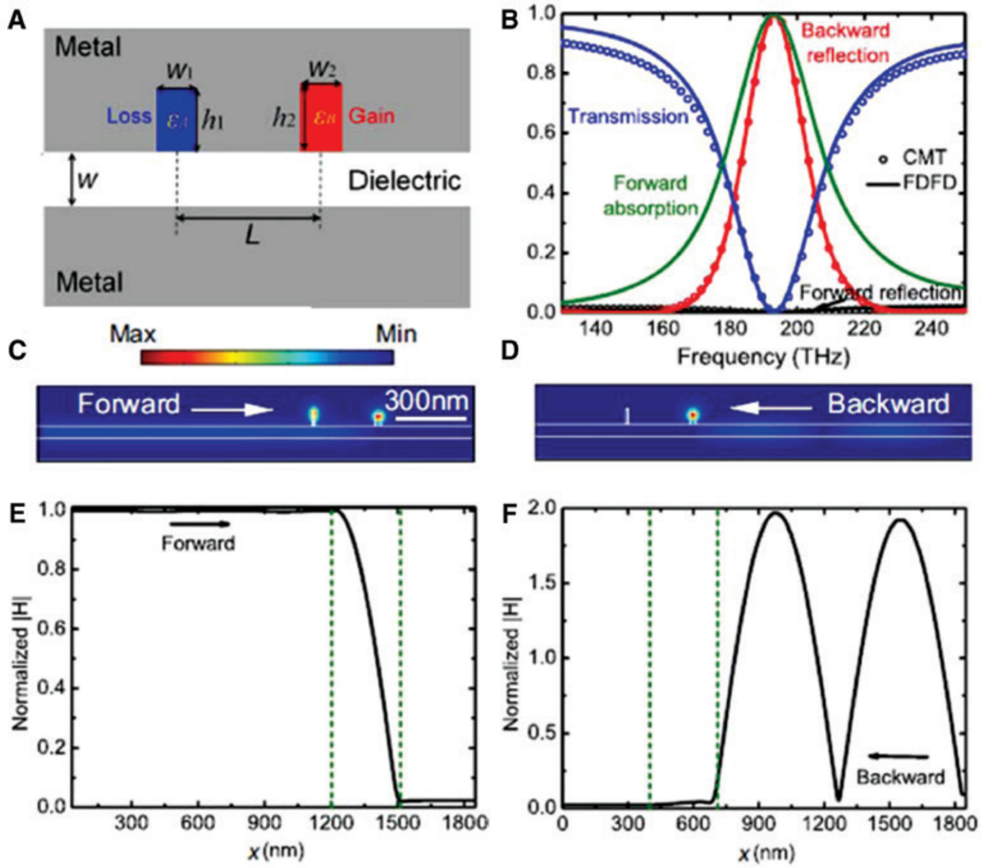

Figure 10: Unidirectional reflectionlessness of a non-*PT*-symmetric system consisting of a MDM plasmonic waveguide side coupled to two MDM stub resonators with unbalanced gain and loss.
(A) Schematic of a perfect absorber unit cell consisting of an MDM plasmonic waveguide side coupled to two MDM stub resonators. (B) Reflection and transmission spectra for the structure of A calculated for light incident from both the forward and backward directions using FDFD (solid lines) and CMT (circles). Results are shown for $w=50$ nm, $w_1=10$ nm, $w_2=25$ nm, $h_1=67.5$ nm, and $h_2=53$ nm. The metal is silver and the dielectric is air. The left and right stubs are filled with SiO_2 doped with CdSe quantum dots ($\varepsilon_A=4.0804-j0.6$) and InGaAsP ($\varepsilon_B=11.38+j0.41$), respectively. Also shown are the absorption spectra in the forward direction calculated using FDFD (green solid line). (C and D) Magnetic field amplitude profiles for the structure of (A) at $f=193.4$ THz ($\lambda_0=1.55$ μm), when the fundamental TM mode of the MDM waveguide is incident from the left and right, respectively. All parameters are as in (B). (E and F) Magnetic field amplitude in the middle of the MDM waveguide, normalized with respect to the field amplitude of the incident fundamental TM waveguide mode in the middle of the waveguide, when the mode is incident from the left and right, respectively. The two vertical dashed lines indicate the left boundary of the left stub and the right boundary of the right stub. All parameters are as in (B) [127].

$$\frac{1}{\tau_2}=\frac{1}{\tau_1}=\frac{1}{\tau},\ \frac{1}{\tau_{01}}=\frac{1}{\tau}(e^{2\alpha L}+1),\ \frac{1}{\tau_{02}}=0,$$
$$\omega_{01}=\omega_{02}=\omega_0,\ \cos(2\beta L)=-1, \tag{8}$$

where ω_{01} and ω_{02} are the resonance frequencies of the two resonators, $1/\tau_i$, $i=1, 2$, are the decay rates of the resonator mode amplitudes due to the power escape through the waveguide, $1/\tau_{0i}$, $i=1, 2$, are the decay (growth) rates due to the internal loss (gain) in the resonators, and L is the distance between the two resonators. α and β are the real and imaginary parts, respectively, of the complex propagation constant of the fundamental mode in the waveguide at $\lambda_0=1.55$ μm. The left and right stubs are filled with SiO_2 doped with CdSe quantum dots ($\varepsilon_A=4.0804-j0.6$) and InGaAsP ($\varepsilon_B=11.38+j0.41$), respectively. The real parts of ε_A and ε_B are fixed, whereas the imaginary parts are tuned to satisfy Equation (8). In Figure 10B, we observe that not only the system exhibits unidirectional reflectionless light propagation at the resonance frequency of $f_0=193.4$ THz ($\lambda_0=1.55$ μm) but also the off-resonance reflection in the forward direction beyond $f_0=193.4$ THz is significantly suppressed in a broad frequency range.

More interestingly, as shown in Figure 10B, the on-resonance reflection in the backward direction is unity. This is due to the fact that the right stub behaves as a lossless stub [$\frac{1}{\tau_{02}}=0$, Equation (8)]; therefore, it acts as a perfect reflector at the resonant frequency ($f_0=193.4$ THz).

The gain of the material filling the right stub compensates the material loss in the metal. Thus, the on-resonance transmission for light incident from both the forward and backward directions is zero, and for light incident from the left, the on-resonance absorption is unity. We note here that the existence of an EP-induced unidirectional reflectionless mode with unity transmission in *PT*-symmetric systems with balanced gain and loss (Figure 2) is commonly referred to as unidirectional invisibility, whereas the existence of an EP-induced unidirectional reflectionless mode with zero transmission corresponds to unidirectional perfect absorption. Ramezani et al. also obtained unidirectional perfect absorption in passive Fano disk resonators at EPs based on a similar idea [130].

The unidirectional perfect absorption in the forward direction can be observed in the magnetic field distributions. When the waveguide mode is incident from the right (backward direction), there is no transmission, and the incident and reflected fields form a strong interference pattern (Figure 10D and F). On the contrary, when the waveguide mode is incident from the left (forward direction), there is hardly any reflection or transmission (Figure 10C and E). In addition, by cascading multiple non-*PT*-symmetric optical structures with different resonant absorption frequencies, and taking advantage of their broadband near-zero reflection property, an ultra-broadband near-total absorber can be realized. It should be noted that the proposed non-*PT*-symmetric waveguide-cavity system can also be realized using other nanophotonic structures such as microring and PhC cavities [131, 132]. In such lossless structures, gain media are not required to implement the proposed waveguide-cavity systems, as there is no internal loss in the resonators.

Recently, Yang et al. performed the first direct measurement of asymmetric backscattering (reflection) in a microcavity. Their setup consists of an erbium-doped silica microtoroid whispering-gallery modes (WGM) resonator that allows for in- and out-coupling of light through two single-mode optical fiber waveguides (Figure 11A) [133]. They have also previously reported *PT*-symmetry breaking in two coupled WGM silica microtoroid resonators with balanced gain and loss [134]. Here, to probe the asymmetric backscattering of the WGMs, they used two silica nanotips as Rayleigh scatterers (Figure 11A). The microcavity is an open system, and the corresponding effective Hamiltonian is

$$H=\begin{pmatrix}\Omega_c & A\\ B & \Omega_c\end{pmatrix}, \tag{9}$$

which is, in general, non-Hermitian. The real parts of the diagonal elements Ω_c are the frequencies, and their imaginary parts are the decay rates of the resonant traveling waves. The complex-valued off-diagonal elements A and B are the backscattering coefficients, which describe the scattering from the clockwise (cw) [counterclockwise (ccw)] to the counterclockwise (clockwise) propagating wave (Figure 11A). The complex eigenvalues of H are

$$\Omega_\pm=\Omega_c\pm\sqrt{AB}, \tag{10}$$

and its eigenvectors are

$$\Psi_\pm=\left(\sqrt{A},\pm\sqrt{B}\right). \tag{11}$$

When the first scatterer is introduced into the WGM volume, frequency splitting (Ω_+ and Ω_-) can be observed in the transmission spectra due to scatterer-induced modal coupling between the cw and ccw propagating modes. Subsequently, the relative position (i.e. relative phase angle β) and the size of the second scatterer are tuned by nanopositioners to bring the system to an EP (Figure 11B), which, as mentioned above, is a non-Hermitian degeneracy identified by the coalescence of the complex frequency eigenvalues (Ω_+ and Ω_-) and the corresponding eigenstates $\Psi_+=\Psi_-$. As a result, asymmetric backscattering (unidirectional reflectionlessness) of the WGMs can be achieved ($A=0$, or $B=0$).

In the absence of scatterers, a resonance peak appears in the transmission and no signal is observed in the reflection (backscattering), when the light is incident from the cw direction, as a result of wave vector matching (Figure 11C-i). Similarly, there is a resonance peak in the transmission and no signal in the reflection when the light is coming from the ccw direction (Figure 11D-i). In the presence of the first scatterer, two split resonance modes are observed in the transmission and reflection spectra regardless of whether the signal is coming from the cw or the ccw direction (Figure 11C-ii and D-ii). This implies that the field inside the resonator is composed of modes propagating in both cw and ccw directions due to the modal coupling between these two modes. Note that reflection in the cw and ccw directions is symmetric (red line in Figure 11C-ii and blue line in Figure 11D-ii). When the second scatterer is introduced and its position and size are tuned to form an EP, the transmission in the two different directions is still symmetric, whereas the reflection is asymmetric (red line in Figure 11C-iii and blue line in Figure 11D-iii). The reflection in the cw direction vanishes, whereas the reflection in the ccw direction supports a resonance peak. This unidirectional zero backscattering phenomenon can support chiral behavior [133, 135–138] and enable directional emission of a WGM microlaser at EPs. It is also noteworthy that the EP in this non-*PT*-symmetric microcavity

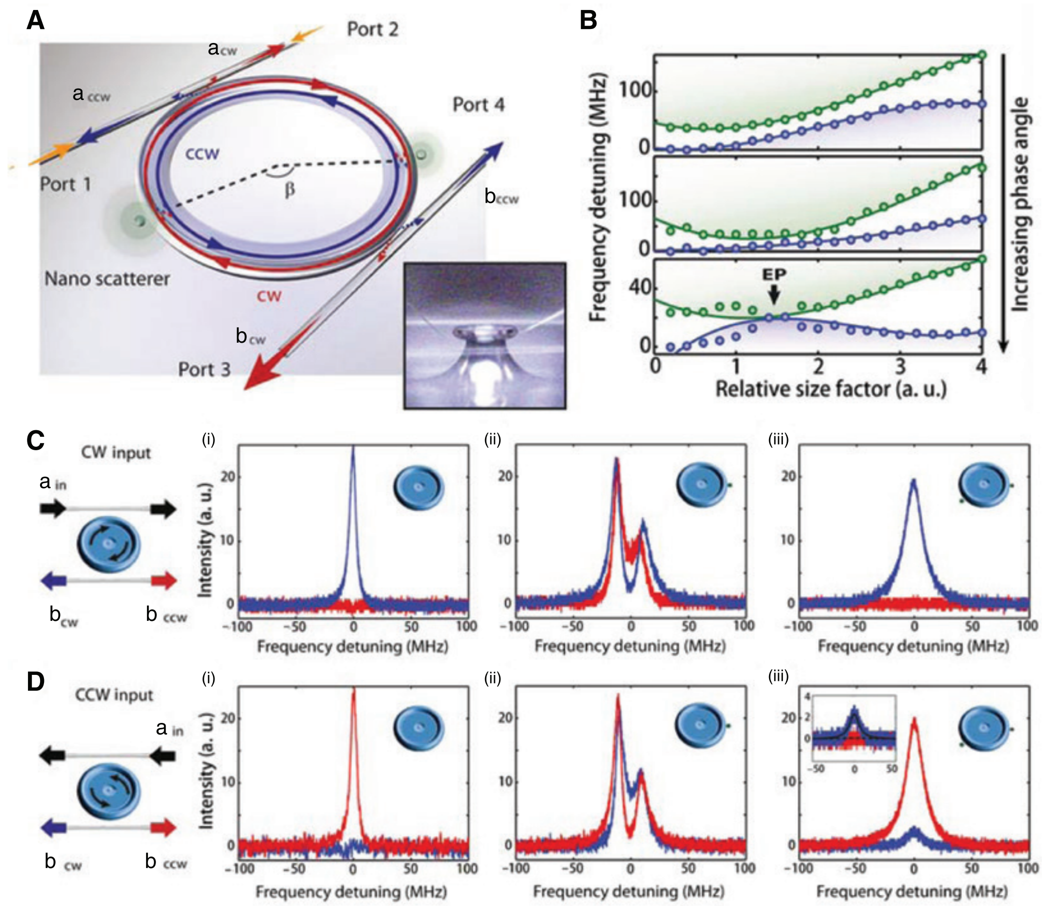

Figure 11: Experimental observation of scatterer-induced asymmetric backscattering in a WGM resonator side-coupled to two waveguides. (A) Illustration of a WGM resonator side-coupled to two waveguides, with the two scatterers enabling the dynamical tuning of the modes. cw and ccw are the clockwise and counterclockwise rotating intracavity fields. $a_{cw(ccw)}$ and $b_{cw(ccw)}$ are the field amplitudes propagating in the waveguides. β is the relative phase angle between the scatterers. Inset shows the optical microscope image of the microtoroid resonator, the tapered fiber waveguides (horizontal lines), and the two silica nanotips denoting the scatterers (diagonal lines on the left and right sides of the resonator). (B) Varying the size and the relative phase angle of a second scatterer helps to dynamically change the frequency detuning (splitting) and the linewidths of the split modes revealing avoided crossings (top) and an EP (bottom). (C and D) When there is no scattering center in or on the resonator, light coupled into the resonator through the first waveguide in the cw (C-i) [or ccw (D-i)] direction couples out into the second waveguide in the cw (C-i) [or ccw (D-i)] direction: the resonant peak in the transmission and no signal in the reflection. (C-ii and D-ii) When a first scatterer is placed in the mode field, resonant peaks are observed in both the transmission and the reflection regardless of whether the light is input in the cw (C-ii) or ccw (D-ii) direction. (C-iii and D-iii) When a second scatterer is suitably placed in the mode field, for the cw input, there is no signal in the reflection output port (C-iii), whereas, for the ccw input, there is a resonant peak in the reflection, revealing asymmetric backscattering for the two input directions. Inset in D-iii compares the two backscattering peaks in C-iii and D-iii [133].

system is induced by tuning of the geometric parameters, such as the size of scatterers and the relative phase angle between scatterers (Figure 11B), rather than tuning of the refractive index of the materials.

4 Conclusions and outlook

Asymmetric light transport is important for several key applications in photonic circuits [19, 64, 138, 139]. In this paper, we reviewed unidirectional reflectionless light propagation at EPs. We first discussed the large body of recent works on unidirectional invisibility using *PT*-symmetric systems with balanced gain and loss. We then discussed how it is possible to achieve one-way zero reflection at EPs through a periodic passive *PT*-symmetric modulation of the dielectric permittivity. When additional material potentials, such as the magnetic permeability, are considered, additional degrees of freedom exist in establishing *PT* symmetry to obtain unidirectional reflectionlessness at EPs. In addition, EPs exist in a larger family of non-Hermitian Hamiltonians. As an example, a medium with a permittivity profile, which is an analytic function in the upper or lower half of the complex position plane, and its real and imaginary parts are related by the spatial Kramers-Kronig relations, shows unidirectional nonreflecting behavior. This finding is more general than previous results associated with *PT* symmetry. The proposed non-*PT*-symmetric optical systems also provide a simple way to realize asymmetric reflection by solely tuning the imaginary part of the permittivity of materials. In addition, systems that exhibit unidirectional perfect absorption have also been demonstrated. We finally reviewed unidirectional reflectionless light propagation at EPs in non-*PT*-symmetric structures through tuning of their geometric parameters rather than the refractive index profiles of the materials. These designs can reduce the difficulty in the experimental realization of such structures.

Unidirectional reflectionless light propagation is an intriguing phenomenon. Based on unidirectional invisibility in acoustics, a noninvasive, shadow-free, fully invisible acoustic sensor with *PT* symmetry was recently demonstrated [140]. Unidirectional invisibility at EPs in optics may also have remarkable implications for noninvasive sensing. In addition, applying unidirectional perfect absorption designs in optical structures based on electro-optic, absorptive, and nonlinear materials with outstanding properties could advance the development of nanophotonic devices, such as switches, modulators, and devices for imaging. In addition, EPs in plasmons could lead to nanoscale photonic devices with novel functionalities.

Acknowledgments: The authors want to acknowledge financial support from the Foundation of the Key Laboratory of Optoelectronic Devices and Systems of the Ministry of Education and Guangdong Province (GD201601), the National Science Foundation (NSF) grants 1102301 and 1254934, the National Natural Science Foundation of China (NSFC) grants 61605252 and 61422506, and the Air Force Office of Scientific Research (AFOSR) grants FA9550-12-1-0471 and FA9550-17-1-0002.

References

[1] Moiseyev N. Non-hermitian quantum mechanics. Cambridge, UK, Cambridge University Press, 2011.
[2] Heiss WD, Sannino AL. Avoided level crossing and exceptional points. J Phys A Math Gen 1990;23:1167–78.
[3] Heiss WD. Repulsion of resonance states and exceptional points. Phys Rev E 2000;61:929–32.
[4] Heiss WD. Exceptional points of non-Hermitian operators. J Phys A Math Gen 2004;37:2455–64.
[5] Berry MV. Physics of nonhermitian degeneracies. Czech J Phys 2004;54:1039–47.
[6] Ryu JW, Son WS, Hwang DU, Lee SY, Kim SW. Exceptional points in coupled dissipative dynamical systems. Phys Rev E 2015;91:052910.
[7] Kirillov ON. Exceptional and diabolical points in stability questions. Fortschr Phys 2013;61:205–24.
[8] Stehmann T, Heiss WD, Scholtz FG. Observation of exceptional points in electronic circuits. J Phys A Math Gen 2004;37:7813–9.
[9] Kammerer M, Merz F, Jenko F. Exceptional points in linear gyrokinetics. Phys Plasmas 2016;15:052102.
[10] Heiss WD. The physics of exceptional points. J Phys A 2012;45:444016.
[11] Bender CM, Boettcher S. Real spectra in non-Hermitian Hamiltonians having *PT*-symmetry. Phys Rev Lett 1998;80:5243.
[12] Lin Z, Ramezani H, Eichelkraut T, Kottos T, Cao H, Christodoulides DN. Unidirectional invisibility induced by *PT*-symmetric periodic structures. Phys Rev Lett 2011;106:213901.
[13] Regensburger A, Bersch C, Miri MA, Onishchukov G, Christodoulides DN, Peschel U. Parity-time synthetic photonic lattices. Nature 2012;488:167–71.
[14] Makris KG, El-Ganainy R, Christodoulides DN, Musslimani ZH. Beam dynamics in *PT* symmetric optical lattices. Phys Rev Lett 2008;100:103904.
[15] Cerjan A, Raman A, Fan S. Exceptional contours and band structure design in parity-time symmetric photonic crystals. Phys Rev Lett 2016;116:203902.
[16] Musslimani ZH, Makris KG, El-Ganainy R, Christodoulides DN. Optical solitons in *PT* periodic potentials. Phys Rev Lett 2008;100:030402.
[17] Ruter CE, Makris KG, El-Ganainy R, Christodoulides DN, Segev M, Kip D. Observation of parity-time symmetry in optics. Nat Phys 2010;6:192–5.
[18] Guo A, Salamo JG, Duchesne D, et al. Observation of *PT*-symmetry breaking in complex optical potentials. Phys Rev Lett 2009;103:093902.
[19] Chang L, Jiang X, Hua S, et al. Parity-time symmetry and variable optical isolation in active-passive-coupled microresonators. Nat Photon 2014;8:524–9.
[20] Zhou X, Chong YD. *PT* symmetry breaking and nonlinear optical isolation in coupled microcavities. Opt Express 2016;24:6919–30.
[21] Longhi S. *PT*-symmetric laser absorber. Phys Rev A 2010;82:031801.
[22] Chong YD, Ge L, Stone AD. *PT*-symmetry breaking and laser-absorber modes in optical scattering systems. Phys Rev Lett 2011;106:093902.
[23] Sun Y, Tan W, Li H, Li J, Chen H. Experimental demonstration of a coherent perfect absorber with *PT* phase transition. Phys Rev Lett 2014;112:143903.
[24] Radi Y, Sounas DL, Alu A, Tretyakov SA. Parity-time-symmetric teleportation. Phys Rev B 2016;93:235427.
[25] Lupu A, Benisty H, Degiron A. Switching using *PT*-symmetry in plasmonic systems: positive role of the losses. Opt Express 2013;21:21651–68.
[26] Savoia S, Castaldi G, Galdi V. Tunneling of obliquely incident waves through *PT*-symmetric epsilon-near-zero bilayers. Phys Rev B 2014;89:085105.

[27] Vysloukh VA, Kartashov YV. Resonant mode conversion in the waveguides with unbroken and broken *PT*-symmetry. Opt Lett 2014;39:5933–6.
[28] Feng S. Loss-induced super scattering and gain-induced absorption. Opt Express 2016;24:1291–304.
[29] Dmitriev SV, Sukhorukov AA, Kivshar YS. Binary parity-time symmetric nonlinear lattices with balanced gain and loss. Opt Lett 2010;35:2976–8.
[30] Miroshnichenko AE, Malomed BA, Kivshar YS. Nonlinearly *PT*-symmetric systems: spontaneous symmetry breaking and transmission resonances. Phys Rev A 2011;84:012123.
[31] Lazarides N, Tsironis GP. Gain-driven discrete breathers in *PT*-symmetric nonlinear metamaterials. Phys Rev Lett 2013;110:053901.
[32] Mostafazadeh A. Spectral singularities of complex scattering potentials and infinite reflection and transmission coefficients at real energies. Phys Rev Lett 2009;102:220402.
[33] Fan S, Baets R, Petrov A, et al. Comment on “Nonreciprocal light propagation in a silicon photonic circuit”. Science 2012;335:38.
[34] Yin X, Zhang X. Unidirectional light propagation at exceptional points. Nat Mater 2013;12:175–7.
[35] Cannata F, Dedonder JP, Ventura A. Scattering in *PT*-symmetric quantum mechanics. Ann Phys 2007;322:397–433.
[36] Choi Y, Kang S, Lim S, et al. Quasieigenstate coalescence in an atom-cavity quantum composite. Phys Rev Lett 2010;104:153601.
[37] Cartarius H, Main J, Wunner G. Exceptional points in atomic spectra. Phys Rev Lett 2007;99:173003.
[38] Ge L, Chong YD, Stone AD. Conservation relations and anisotropic transmission resonances in one-dimensional *PT*-symmetric photonic heterostructures. Phys Rev A 2012;85:023802.
[39] Longhi S. Invisibility in *PT*-symmetric complex crystals. J Phys A Math Theor 2011;44:485302.
[40] Jackson JD. Classical electrodynamics. New York, Wiley, 2007.
[41] Sarisaman M. Unidirectional reflectionlessness and invisibility in the TE and TM modes of a *PT*-symmetric slab system. Phys Rev A 2017;95:013806.
[42] Kalish S, Lin Z, Kottos T. Light transport in random media with *PT* symmetry. Phys Rev A 2012;85:055802.
[43] Midya B. Supersymmetry-generated one-way-invisible *PT*-symmetric optical crystals. Phys Rev A 2012;89:032116.
[44] Fu Y, Xu Y, Chen H. Zero index metamaterials with *PT* symmetry in a waveguide system. Opt Express 2016;24:1648–57.
[45] Rivolta NXA, Maes B. Side-coupled resonators with parity-time symmetry for broadband unidirectional invisibility. Phys Rev A 2016;94:053854.
[46] Fleury R, Sounas DL, Alu A. Negative refraction and planar focusing based on parity-time symmetric metasurfaces. Phys Rev Lett 2014;113:023903.
[47] Hahn C, Choi Y, Yoon JW, Song SH, Oh CH, Berini P. Observation of exceptional points in reconfigurable non-Hermitian vector-field holographic lattices. Nat Commun 2016;7:12201.
[48] Yang F, Mei Z. Guiding SPPs with *PT*-symmetry. Sci Rep 2015;5:14981.
[49] Ritchie RH. Plasma losses by fast electrons in thin films. Phys Rev 1957;106:874.
[50] Schuller JA, Barnard ES, Cai WS, Jun YC, White JS, Brongersma ML. Plasmonics for extreme light concentration and manipulation. Nat Mater 2010;9:193–204.
[51] Hecht B, Bielefeldt H, Novotny L, Inouye Y, Pohl DW. Local excitation, scattering, and interference of surface plasmons. Phys Rev Lett 1996;77:1889.
[52] Pendry J. Playing tricks with light. Science 1999;285:1687–8.
[53] Soukoulis CM, Koschny T, Tassin P, Shen N, Dastmalchi B. What is a good conductor for metamaterials or plasmonics. Nanophotonics 2015;4:69–74.
[54] Atwater HA, Polman A. Plasmonics for improved photovoltaic devices. Nat Mater 2010;9:205–13.
[55] Liu Z, Mu H, Xiao S, et al. Pulsed lasers employing solution-processed plasmonic Cu3-xP colloidal nanocrystals. Adv Mater 2016;28:3535–42.
[56] Ye C, Liu K, Soref RA, Sorger VJ. A compact plasmonic MOS-based 2×2 electro-optic switch. Nanophotonics 2015;4:261–8.
[57] Li J, Liang S, Xiao S, et al. Four-wave mixing signal enhancement and optical bistability of a hybrid metal nanoparticle-quantum dot molecule in a nanomechanical resonator. Opt Express 2016;24:2360–9.
[58] Yang Z, Antosiewicz TJ, Shegai T. Role of material loss and mode volume of plasmonic nanocavities for strong plasmon-exciton interactions. Opt Express 2016;24:20373–81.
[59] Chen K, Leong ESP, Rukavina M, Nagao T, Liu Y, Zheng Y. Active molecular plasmonics: tuning surface plasmon resonances by exploiting molecular dimensions. Nanophotonics 2015;4:186–97.
[60] Zhu X, Feng L, Zhang P, Yin X, Zhang X. One-way invisible cloak using parity-time symmetric transformation optics. Opt Lett 2013;38:2821–4.
[61] Ramezani H, Li H, Wang Y, Zhang X. Unidirectional spectral singularities. Phys Rev Lett 2014;113:263905.
[62] Jin L, Zhang XZ, Zhang G, Song Z. Reciprocal and unidirectional scattering of parity-time symmetric structures. Sci Rep 2016;6:20976.
[63] Feng L, Wong ZJ, Ma R, Wang Y, Zhang X. Single-mode laser by parity-time symmetry breaking. Science 2014;346:972–5.
[64] Wong ZJ, Xu Y, Kim J, et al. Lasing and anti-lasing in a single cavity. Nat Photon 2016;10:796–801.
[65] Kim KH, Hwang MS, Kim HR, Choi JH, No YS, Park HG. Direct observation of exceptional points in coupled photonic-crystal lasers with asymmetric optical gains. Nat Commun 2016;7:13893.
[66] Hodaei H, Miri MA, Heinrich M, Christodoulides DN, Khajavikhan M. Parity-time-symmetric microring lasers. Science 2014;346:975–8.
[67] Hodaei H, Miri MA, Hassan AU, et al. Single mode lasing in transversely multi-moded *PT*-symmetric microring resonators. Laser Photon Rev 2016;10:494–9.
[68] Feng L, Xu Y, Fegadolli WS, et al. Experimental demonstration of a unidirectional reflectionless parity-time metamaterial at optical frequencies. Nat Mater 2013;12:108–13.
[69] Zhao H, William SF, Yu J, et al. Metawaveguide for asymmetric interferometric light-light switching. Phys Rev Lett 2016;117:193901.
[70] Zhang J, MacDonald KF, Zheludev NI. Controlling light-with-light without nonlinearity. Light Sci Appl 2012;1:e18.
[71] Fang X, MacDonald KF, Zheludev NI. Controlling light with light using coherent metadevices: all-optical transistor, summator and invertor. Light Sci Appl 2015;1:e292.
[72] Lan S, Kang L, Schoen DT, et al. Backward phase-matching for nonlinear optical generation in negative-index materials. Nat Mater 2015;14:807–12.

[73] Volz T, Reinhard A, Winger M, et al. Ultrafast all-optical switching by single photons. Nat Photon 2012;6:605–9.
[74] Englund D, Majumdar A, Bajcsy M, Faraon A, Petroff P, Vuckovic J. Ultrafast photon-photon interaction in a strongly coupled quantum dot-cavity system. Phys Rev Lett 2012;108:093604.
[75] Jia Y, Yan Y, Kesava SV, Gomez ED, Giebink NC. Passive parity-time symmetry in organic thin film waveguides. ACS Photo 2015;2:319–25.
[76] Rosenblatt D, Sharon A, Friesem AA. Resonant grating waveguide structures. IEEE J Quantum Electron 1997;33: 2038–59.
[77] Yan Y, Giebink NC. Passive *PT* symmetry in organic composite films via complex refractive index modulation. Adv Opt Mater 2014;2:423–7.
[78] Zhu X, Xu Y, Zou Y, et al. Asymmetric diffraction based on a passive parity-time grating. Appl Phys Lett 2016;109:111101.
[79] Dai D, Shi Y, He S, Wosinski L, Thylen L. Gain enhancement in a hybrid plasmonic nano-waveguide with a low-index or high-index gain medium. Opt Express 2011;19:12925–36.
[80] Yu Z, Veronis G, Fan S. Gain-induced switching in metal-dielectric-metal plasmonic waveguides. Appl Phys Lett 2008;92:041117.
[81] García-Blanco SM, Pollnau M, Bozhevolnyi SI. Loss compensation in long-range dielectric-loaded surface plasmon-polariton waveguides. Opt Express 2011;19:25298–311.
[82] Berini P, Leon ID. Surface plasmon-polariton amplifiers and lasers. Nat Photon 2011;6:16–24.
[83] Li D, Feng J, Pacifici D. Higher-order surface plasmon contributions to passive and active plasmonic interferometry. Opt Express 2016;24:27309–18.
[84] Hahn C, Song SH, Oh CH, Berini P. Single-mode lasers and parity-time symmetry broken gratings based on active dielectric-loaded long-range surface plasmon polariton waveguides. Opt Express 2015;23:19922–31.
[85] Kulishov M, Kress B, Slavík R. Resonant cavities based on parity-time-symmetric diffractive gratings. Opt Express 2013;21:9473–83.
[86] Castaldi G, Savoia S, Galdi V, Alu A, Engheta N. *PT* metamaterials via complex-coordinate transformation optics. Phys Rev Lett 2013;110:173901.
[87] Gear J, Liu F, Chu ST, Rotter S, Li J. Parity-time symmetry from stacking purely dielectric and magnetic slabs. Phys Rev A 2015;91:033825.
[88] Mejıa-Cortes C, Molina MI. Interplay of disorder and *PT* symmetry in one-dimensional optical lattices. Phys Rev A 2015;113:033815.
[89] Ding K, Zhang Q, Chan CT. Coalescence of exceptional points and phase diagrams for one-dimensional *PT*-symmetric photonic crystals. Phys Rev A 2015;92:235310.
[90] Ge L, Tureci HE. Antisymmetric *PT*-photonic structures with balanced positive- and negative-index materials. Phys Rev A 2013;88:053810.
[91] Wu J, Artoni M, La Rocca GC. Non-Hermitian degeneracies and unidirectional reflectionless atomic lattices. Phys Rev Lett 2014;113:123004.
[92] Wu J, Artoni M, La Rocca GC. Parity-time-antisymmetric atomic lattices without gain. Phys Rev A 2015;91:033811.
[93] Szameit A, Rechtsman MC, Bahat-Treidel O, Segev M. *PT*-symmetry in honeycomb photonic lattice. Phys Rev A 2011;84:021806(R).
[94] Ramezani H, Kottos T, Kovanis V, Christodoulides DN. Exceptional-point dynamics in photonic honeycomb lattices with *PT* symmetry. Phys Rev A 2012;85:013818.
[95] Zhen B, Hsu CW, Igarashi Y, et al. Spawning rings of exceptional points out of Dirac cones. Nature 2015;525:354–8.
[96] Lin Z, Pick A, Loncar M, Rodriguez AW. Enhanced spontaneous emission at third-order Dirac exceptional points in inverse-designed photonic crystals. Phys Rev Lett 2016;117:117402.
[97] Turduev M, Botey M, Giden I, et al. Two-dimensional complex parity-time-symmetric photonic structures. Phys Rev A 2015;91:203825.
[98] Mock A. Parity-time-symmetry breaking in two-dimensional photonic crystals: square lattice. Phys Rev A 2016;93: 063812.
[99] Mostafazadeh A. Invisibility and *PT* symmetry. Phys Rev A 2013;87:012103.
[100] Horsley SAR, Artoni M, La Rocca GC. Spatial Kramers-Kronig relations and the reflection of waves. Nat Photon 2015;9: 436–9.
[101] Lucarini V, Bassani F, Peiponen KE, Saarinen JJ. Dispersion theory and sum rules in linear and nonlinear optics. Riv Nuovo Cimento 2003;26:1–120.
[102] Feng L, Zhu X, Yang S, et al. Demonstration of a large-scale optical exceptional point structure. Opt Express 2014;22:1760–7.
[103] Yariv A, Yeh P. Photonics: optical electronics in modern communications. New York, Oxford University Press, 2007.
[104] Shen Y, Deng X, Chen L. Unidirectional invisibility in a two-layer non-*PT*-symmetric slab. Opt Express 2014;22:19440–7.
[105] Ge L, Feng L. Optical-reciprocity-induced symmetry in photonic heterostructures and its manifestation in scattering *PT*-symmetry breaking. Phys Rev A 2016;94:043836.
[106] Kang M, Cui H, Li T, Chen J, Zhu W, Premaratne M. Unidirectional phase singularity in ultrathin metamaterials at exceptional points. Phys Rev A 2014;89:065801.
[107] Huang Y, Veronis G, Min C. Unidirectional reflectionless propagation in plasmonic waveguide-cavity systems at exceptional points. Opt Express 2015;23:29882–95.
[108] Nath J, Modak S, Rezadad I, et al. Far-infrared absorber based on standing-wave resonances in metal-dielectric-metal cavity. Opt Express 2015;23:20366–80.
[109] Cao G, Li H, Deng Y, Zhan S, He Z, Li B. Plasmon-induced transparency in a single multimode stub resonator. Opt Express 2014;22:25215–23.
[110] Huang Y, Min C, Dastmalchi P, Veronis G. Slow-light enhanced subwavelength plasmonic waveguide refractive index sensors. Opt Express 2015;23:14922–36.
[111] Zhan S, Li H, He Z, Li B, Chen Z, Xu H. Sensing analysis based on plasmon induced transparency in nanocavity-coupled waveguide. Opt Express 2015;23:20313–20.
[112] Blanchard-Dionne A, Meunier M. Optical transmission theory for metal-insulator-metal periodic nanostructures. Nanophotonics 2017;6:349–55.
[113] Shin W, Fan S. Unified picture of modal loss rates from microwave to optical frequencies in deep-subwavelength metallic structures: a case study with slot waveguides. Appl Phys Lett 2015;107:171102.
[114] Hu B, Zhang Y, Wang Q. Surface magneto plasmons and their applications in the infrared frequencies. Nanophotonics 2015;4:383–96.

[115] Neutens P, Dorpe V, De Vlaminck I, Lagae L, Borghs G. Electrical detection of confined gap plasmons in metal-insulator-metal waveguides. Nat Photon 2009;3:283–6.
[116] Huang Y, Min C, Tao S, Veronis G. Design of compact Mach-Zehnder interferometer based slow light enhanced plasmonic waveguide sensors. J Lightw Technol 2016;34:2796–803.
[117] Economou EN. Surface plasmons in thin films. Phys Rev 1969;182:539–54.
[118] Salamin Y, Heni W, Haffner C, et al. Direct conversion of free space millimeter waves to optical domain by plasmonic modulator antenna. Nano Lett 2015;15:8342–6.
[119] Yang X, Hu X, Yang H, Gong Q. Ultracompact all-optical logic gates based on nonlinear plasmonic nanocavities. Nanophotonics 2017;6:365–76.
[120] Huang Y, Veronis G. Compact slit-based couplers for metal-dielectric-metal plasmonic waveguides. Opt Express 2012;20:22233–44.
[121] Kocabas SE, Veronis G, Miller DAB, Fan S. Transmission line and equivalent circuit models for plasmonic waveguide components. IEEE J Sel Top Quantum Electron 2008;14:1462–72.
[122] Huang Y, Min C, Veronis G. Subwavelength slow-light waveguides based on a plasmonic analogue of electromagnetically induced transparency. Appl Phys Lett 2011;99:143117.
[123] Kekatpure RD, Barnard ES, Cai W, Brongersma ML. Phase coupled plasmon induced transparency. Phys Rev Lett 2010;104:243902.
[124] Shin W, Cai W, Catrysse PB, Veronis G, Brongersma ML, Fan S. Broadband sharp 90-degree bends and T-splitters in plasmonic coaxial waveguides. Nano Lett 2013;13:4753–8.
[125] Mahigir A, Dastmalchi P, Shin W, Fan S, Veronis G. Plasmonic coaxial waveguide-cavity devices. Opt Express 2015;23:20549–62.
[126] Yang E, Lu Y, Wang Y, Dai Y, Wang P. Unidirectional reflectionless phenomenon in periodic ternary layered material. Opt Express 2016;24:14311–21.
[127] Huang Y, Min C, Veronis G. Broadband near total light absorption in non-*PT*-symmetric waveguide-cavity systems. Opt Express 2016;24:22219–31.
[128] Wang K, Yu Z, Sandhu S, Fan S. Fundamental bounds on decay rates in asymmetric single-mode optical resonators. Opt Lett 2013;38:100–2.
[129] Manolatou C, Khan MJ, Fan S, Villeneuve PR, Haus HA, Joannopoulos JD. Coupling of modes analysis of resonant channel add-drop filters. IEEE J Sel Top Quantum Electron 1999;35:1322–31.
[130] Ramezani H, Wang Y, Yablonovitch E, Zhang X. Unidirectional perfect absorber. IEEE J Sel Top Quantum Electron 2016;22:5000706.
[131] Xia F, Sekaric L, Vlasov Y. Ultracompact optical buffers on a silicon chip. Nat Photon 2007;1:65–71.
[132] Notomi M, Kuramochi E, Tanabe T. Large-scale arrays of ultrahigh-Q coupled nanocavities. Nat Photon 2008;2:741–7.
[133] Peng B, Ozdemir SK, Liertzer M, et al. Chiral modes and directional lasing at exceptional points. Proc Natl Acad Sci U S A 2016;113:6845–50.
[134] Peng B, Ozdemir SK, Lei F, et al. Parity-time-symmetric whispering gallery microcavities. Nat Phys 2014;10:394–8.
[135] Wiersig J. Structure of whispering-gallery modes in optical microdisks perturbed by nanoparticles. Phys Rev A 2011;84:063828.
[136] Dembowski C, Dietz B, Graf HD, et al. Observation of a chiral state in a microwave cavity. Phys Rev Lett 2003;90:034101.
[137] Heiss WD, Harney HL. The chirality of exceptional points. Eur Phys J D 2001;17:149–51.
[138] Shen Y, Bradford M, Shen JT. Single-photon diode by exploiting the photon polarization in a waveguide. Phys Rev Lett 2011;107:173902.
[139] Alaeian H, Dionne JA. Non-Hermitian nanophotonic and plasmonic waveguides. Phys Rev B 2014;89:075136.
[140] Fleury R, Sounas D, Alu A. An invisible acoustic sensor based on parity-time symmetry. Nat Commun 2015;6:5905.